Skeletal Muscle TFEB Signaling Promotes Central Nervous System Function and Reduces Neuroinflammation during Aging and Neurodegenerative Disease

Ian Matthews [1,2]

Allison Birnbaum [1,2]

Anastasia Gromova [3]

Amy W. Huang [1,2]

Kailin Liu [1,2]

Eleanor A. Liu [1,2]

Kristen Coutinho [5]

Megan McGraw [6]

Dalton C. Patterson [6]

Macy T. Banks [6]

Amber C. Nobles [7]

Nhat Nguyen [3]

Gennifer E. Merrihew [8]

Lu Wang [9]

Eric Baeuerle [10-12]

Elizabeth Fernandez [10-12]

Nicolas Musi [13]

Michael J. MacCoss [8]

21 Helen C. Miranda [14-16]

22 * Albert R. La Spada [3,4] (co-corresponding author)*

23 Constanza J. Cortes [1,2] (corresponding author)

24 [1] Leonard Davis School of Gerontology, [2] University of Southern California, [3] Department of
25 Pathology and Laboratory Medicine, University of California, Irvine, [4] Department of Neurology
26 and Department of Biological Chemistry, UCI Institute for Neurotherapeutics, University of
27 California, Irvine, [5] Comprehensive Diabetes Center, University of Alabama at Birmingham, [6]
28 Department of Cell, Developmental and Integrative Biology, University of Alabama at
29 Birmingham, [7] Department of Neurology, University of Alabama at Birmingham, [8] Department of
30 Genome Sciences, University of Washington , [9] Department of Environmental and Occupational
31 Health Sciences, University of Washington, [10] Department of Pharmacology, [11] Barshop Institute
32 for Longevity and Aging Studies, University of Texas Health San Antonio; [12] Geriatric Research,
33 Education and Clinical Center, South Texas Veterans Health Care Network, San Antonio TX
34 USA [13] Department of Medicine, Cedars-Sinai Medical Center, [14] Department of Genetics and
35 Genome Sciences, School of Medicine, Case Western University, [15] Department of
36 Neurosciences, School of Medicine, Case Western Reserve University, [16] RNA Center, School
37 of Medicine, Case Western Reserve University,

38 **Funding**: NIH R01 AG077536 (CJC), University of Washington Nathan Shock Center P30
39 AG013280 (Pilot Grant to CJC), San Antonio Nathan Shock Center of Excellence in the Basic
40 Biology of Aging P30AG013319 (Pilot Grant to CJC), NIH R35 122140 (ALS).

41 **Acknowledgements**: We thank members of the lab past and present, as well as former and
42 current colleagues and collaborators for their helpful contributions.

Summary

Skeletal muscle has recently arisen as a novel regulator of Central Nervous System (CNS) function and aging, secreting bioactive molecules known as myokines with metabolism-modifying functions in targeted tissues, including the CNS. Here we report the generation of a novel transgenic mouse with enhanced skeletal muscle lysosomal and mitochondrial function via targeted overexpression of Transcription Factor E-B (TFEB). We have discovered that the resulting geroprotective effects in skeletal muscle reduce neuroinflammation and the accumulation of tau-associated pathological hallmarks in a mouse model of tau pathology. Muscle-specific TFEB overexpression also significantly ameliorates proteotoxicity, reduces neuroinflammation and promotes transcriptional remodeling of the aged CNS, preserving cognition and memory in aged mice. Our results implicate the maintenance of skeletal muscle function throughout aging to direct regulation of CNS health and disease, and suggest that skeletal-muscle originating factors may act as novel therapeutic targets against age-associated neurodegenerative disorders.

INTRODUCTION

Aging is associated with an organism-wide progressive loss of tissue form and function, broadly characterized by the 'hallmarks of aging' [1]. In particular, the aging central nervous system (CNS) [1,2] exhibits a global loss in protein homeostasis (proteostasis), impaired neuroplasticity and resilience, and an increase in neuroinflammation [2,3]. These alterations are believed to render the aging CNS vulnerable to age-associated dysfunction and the development of neurodegenerative disease [2].

Over the last ten years, there has been growing evidence that suggests prominent contributions of the periphery to the etiology of age-associated neurodegenerative diseases [4-8]. In particular, manipulation of skeletal muscle protein quality control pathways yields important benefits to the invertebrate CNS, protecting against the accumulation of aggregation-prone neurodegenerative disease proteins in the brain and the retina [5,8,9]. Although the mechanisms responsible for these benefits remain poorly understood, some of these effects are mediated by secreted factors that communicate metabolic and inflammatory signals between tissues [5,7,9]. In agreement with this, blood circulating factors have recently arisen as potent regulators of mammalian CNS aging and metabolism [10-13]. For example, exposure to a young plasma environment (either through heterochronic parabiosis or plasma transfers) can rescue function in the aging CNS [12-14] by decreasing neuroinflammation [15] and enhancing neurogenesis [10]. Studies have further demonstrated that increasing the levels of these individual factors in peripheral circulation is sufficient to rejuvenate the aged CNS [12,16,17], supporting the existence of geroprotective circulating factors with CNS targeting effects. Although the source and identity of these neuroprotective circulating cytokines are unclear, several of them are expressed in, and are known to be secreted from, skeletal muscle [5,18-20]. In fact, skeletal muscle acts as an endocrine organ, secreting a myriad of bioactive factors that induce metabolic changes in a non-cell autonomous manner in distant tissues like liver [21], adipose tissue [22], and the CNS [19].

Recently, this muscle-to-brain signaling axis has been proposed to have important implications for CNS aging and age-associated neurodegenerative disease [19,23,24]. Indeed, skeletal muscle function has arisen as a key predictor for phenotypic and clinical outcomes in age-associated neurodegenerative diseases, including Alzheimer's Disease (AD) and Parkinson's Disease (PD) [25,26]. Consistent with this, we were the first to uncover a novel mechanistic basis for motor neuron disease in the polyglutamine disease Spinal and Bulbar Muscular Atrophy (SBMA), where disruption of skeletal muscle autophagy initiates the pathogenic cascade that culminates

in neuronal toxicity and death [27]. Furthermore, we demonstrated that rescuing proteotoxicity specifically in skeletal muscle was sufficient to rescue motor neuron degeneration and extend lifespan in this model, despite robust misfolded protein burden in the brain [28]. We also demonstrated the feasibility and efficacy of peripheral delivery of antisense oligonucleotides reducing skeletal muscle expression of the misfolded protein in rescuing neurological phenotypes [29], confirming that therapeutic targeting of skeletal muscle can have important benefits to the CNS.

Skeletal muscle metabolism is regulated in part by Transcription Factor E-B (TFEB), a master regulator of a lysosomal-to-nucleus signaling axis that integrates cellular metabolism and lysosomal function [30-32]. TFEB expression and function are strongly induced in skeletal muscle in response to interventions with documented neuroprotective effects on the aging [33,34] and neurodegenerative disease-afflicted CNS, including low nutrient conditions [35] and exercise [36]. Indeed, TFEB controls metabolic flexibility in muscle during exercise, inducing the expression of genes involved in mitochondrial biogenesis, fatty acid oxidation, and oxidative phosphorylation [36]. This coordinated action optimizes mitochondrial substrate utilization, enhancing ATP production and exercise capacity [36]. These findings identify TFEB as a critical mediator of the beneficial effects of exercise on metabolism. However, the precise role of TFEB-dependent signaling in skeletal muscle during aging, and its impact on the muscle-to-brain axis, remains largely unknown.

Here we report the generation of a novel transgenic mouse with enhanced muscle metabolism via overexpression of TFEB. We have discovered that the resulting enhanced skeletal muscle lysosomal function is maintained throughout the lifespan, protecting against the onset of age-associated mitochondrial dysfunction in aging skeletal muscle. Furthermore, we report that overexpression of TFEB in skeletal muscle significantly reduces hippocampal accumulation of neuropathological hallmarks and reduces neuroinflammation in a mouse model of tau pathology, despite no exogenous activation of the transgene in the CNS. Muscle TFEB overexpression also ameliorates proteotoxicity, reduces neuroinflammation, and promotes transcriptional remodeling of the aged CNS without neurodegenerative disease burden, preserving cognitive performance in healthy aging mice. Our results implicate, for the first time in mammals, maintenance of skeletal muscle function to direct regulation of CNS health, and suggest that skeletal-muscle originating factors may act as novel therapeutic targets against age-associated neurodegenerative diseases.

RESULTS

TFEB overexpression maintains fiber type composition, function, and metabolism-associated networks in aging skeletal muscle

We derived a novel line of conditional transgenic mice carrying the β-actin promoter in combination with the CMV enhancer (CAGGS) and with a floxed 3x-FLAG-eGFP STOP cassette placed just 5' to a 3x-FLAG-human *TFEB* transgene (i.e. fxSTOP-TFEB transgenic mice) (**Figure 1A**). In the presence of Cre-recombinase, the STOP codon cassette will be excised out, allowing expression of the human TFEB transgene, also known as a Cre-loxP ON system. To drive overexpression of TFEB specifically in skeletal muscle, we crossed male fxSTOP-TFEB mice with female Human Skeletal Actin (HSA)-Cre mice to achieve widespread expression of Cre-recombinase in cells of the myogenic lineage [37].

The resulting cTFEB;HSACre bigenic mice of both sexes exhibited a strong induction of human *TFEB mRNA* expression in skeletal muscle tissue (**Supplemental Figure 1A, quadriceps**). This exogenous *TFEB* expression was still prominent at 24 months of age in cTFEB;HSACre transgenic skeletal muscle (**Supplemental Figure 1B, quadriceps)** suggesting that overexpression of the transgene remains active even at very old ages. Immunoblotting of quadricep skeletal muscle confirmed robust expression of 3x-FLAG-TFEB protein in cTFEB;HSACre bigenic muscle lysates of both sexes (**Figure 1B**). Human TFEB protein levels in male cTFEB;HSACre mice amounted to about 2-fold higher levels than their female littermates at both ages examined. Importantly, and in agreement with our qRT-PCR studies, human TFEB was still robustly expressed at 24 months of age in both sexes, suggesting life-long expression of our transgene upon embryonic recombination (**Figure 1B**). As TFEB is a transcription factor, we confirmed nuclear localization of human TFEB in cTFEB;HSA-Cre skeletal muscle myonuclei via immunofluorescence (**Supplemental Figure 1C, in white**).

Next, we confirmed TFEB protein overexpression exclusively in skeletal muscle of cTFEB;HSACre bigenic mice by multiple approaches. First, we confirmed expression of the biologically inert 3x-FLAG-eGFP cassette upstream of the STOP codon (**Figure 1A**) and no exogenous expression of 3x-FLAG-TFEB in other highly metabolic tissues of non-myogenic lineages in cTFEB;HSACre transgenic mice, including brown adipose tissue (**Supplemental Figure 1D**) and liver (**Supplemental Figure 1E**). We detected a relatively mild expression of human *TFEB* mRNA levels in the heart of cTFEB;HSACre transgenic mice, confirming previous

152 reports indicating low-level cross-over into cardiac tissue in the HSA-Cre model. However, this
153 expression amounted to about ~400-fold less in young animals and ~15-fold less in aged
154 animals than that detected in skeletal muscle at the same ages (**Supplemental Figure 1A,**
155 **ventricles**). Importantly, we could not detect 3x-FLAG-TFEB protein via immunoblotting in
156 cTFEB;HSACre heart ventricle lysates (**Supplemental Figure 1F**). This suggests that despite
157 some HSA-Cre 'leakiness' into cardiac muscle, synthesis of exogenous TFEB protein in heart
158 tissue is below detectable levels, confirming the high skeletal muscle tropism of HSA-Cre driven
159 expression. Finally, we also did not detect expression of exogenous human TFEB mRNA in the
160 hippocampus (**Supplemental Figure 1A & 1B, hippocampus**) or hemibrain protein lysates
161 (**Supplemental Figure 1G**). To further confirm no CNS expression of transgenes associated
162 with the HSA-Cre driver line, we directly assessed the Cre-mediated recombination of an
163 additional transgene reporter in TdTomato Ai9;HSACre mice. We confirmed robust tdTomato
164 fluorescence in skeletal muscle (**Supplemental Figure 1H**) but no detectable TdTomato
165 fluorescence in the CNS (**Supplemental Figure 1I**), including the hippocampus (**Supplemental**
166 **Figure 1I, insets**), of TdTomato Ai9;HSACre mice, consistent with the muscle-restricted
167 specificity of this HSA-Cre-loxP-ON approach [38]. Overall, these data confirm previous reports of
168 striated muscle-specific Cre-mediated recombination using the HSA-Cre transgenic driver line
169 [37], and demonstrate detectable expression of human TFEB protein only in skeletal muscle of
170 cTFEB;HSACre bigenic mice. This establishes our newly developed inducible fxSTOP-TFEB
171 mouse as an effective model to generate spatiotemporally controlled transgenic expression of
172 human TFEB.

173 Analysis of skeletal muscle wet weight, a proxy for skeletal muscle size, revealed trends
174 towards larger muscle wet weights in young cTFEB;HSACre animals, and a robust and
175 significant preservation of quadriceps and gastrocnemius skeletal muscle wet weight in aged
176 (22–24 month-old) transgenic mice of both sexes (**Figure 1C-D**). Indeed, while control animals
177 lost around 20-30% of their quadriceps wet weight during aging, there was no significant
178 differences between young or aged cTFEB;HSACre skeletal muscle weight (**Figure 1C-D**).
179 Interestingly, this maintenance of muscle wet weight was not associated with changes in total
180 body weight at either age examined (**Figure 1E**). Consistent with these findings, we determined
181 that overexpression of TFEB significantly decreases the number of small fibers (<1500 μm^2) and
182 increases the number of large fibers (>1500 μm^2) in young gastrocnemius skeletal muscle of
183 both sexes (**Figure 1F-G**). This was accompanied by an increase in abundance of type 1 (~1%
184 more) and type 2A (~9% more) fibers (**Figure 1H-K**) and an increase in the cross-sectional area

185 (CSA) of Type 2B (~200 um^2 larger) and 2X (~300 um^2 larger) fibers with no changes in Feret's
186 minimum diameter (**Supplemental Figure 2A-H)**, which was prevalent in male mice and
187 trending in female mice. Importantly, while control male gastrocnemius muscle lost a significant
188 portion of their large fibers during aging, they were not altered in aged male cTFEB:HSACre
189 transgenic muscle (**Figure 1F-G**). The abundance of Type 1 and Type 2A fibers was also still
190 prevalent in aged male cTFEB:HSACre transgenic muscle (**Figure 1H-K and Supplemental**
191 **Figure 2G-H)**, suggesting that TFEB overexpression remodels both fast-twitch glycolytic and
192 oxidative fiber fibers and that these changes are maintained during aging**.** To determine the
193 physiological effects of this fiber type switch on skeletal muscle function, we examined exercise
194 performance in all of our cohorts. We determined that at 6 months of age, muscle-TFEB
195 overexpressing mice had a 20% (males) and 40% (females) longer maximum running distance
196 to exhaustion (**Figure 1L**) and engaged in more total work (**Figure 1M**) than their control
197 littermates. Importantly, this increased enhanced physical performance was still present in aged
198 female cTFEB;HSACre transgenic mice (**Figure 1M**). Taken together, these results suggest that
199 lifelong-expression of TFEB prevents fiber type atrophy and alters fiber type switching in aging
200 skeletal muscle, ultimately preserving muscle size and running performance during aging.

201 Given the principal role of TFEB-regulated signaling (i.e. lysosomal and mitochondrial function)
202 to skeletal muscle health [39,40], as well as the profound geroprotective effects of TFEB
203 overexpression on muscle fiber types, muscle size and exercise performance in aging muscle
204 (**Figure 1**), we sought to examine the overall changes in the skeletal muscle protein landscape
205 in response to TFEB overexpression throughout aging. We performed proteome profiling of
206 young and aged, control and cTFEB;HSACre male quadricep skeletal muscle. Differential
207 abundance analysis of species revealed 909 proteins associated with TFEB overexpression in
208 young (6-month-old) skeletal muscle (**Figure 2A**). Of these, 857 (~94%) were significantly
209 overrepresented and 52 (~6%) were underrepresented compared to their littermate controls. At
210 18 months of age, a time point where age-associated dysfunction is prevalent in murine skeletal
211 muscle [41], the same proteomics approach identified 351 differentially expressed proteins in
212 TFEB-expressing skeletal muscle (**Figure 2B**). Of these, 283 proteins (~81%) were significantly
213 enriched and 68 proteins (~19%) were significantly decreased in cTFEB;HSACre bigenic
214 muscle, with only 53 of these proteins being uniquely expressed in older mice. Importantly, at
215 both ages examined, TFEB remained significantly overexpressed (**Figure 2A & 2B, boxes**),
216 confirming our previous finding that exogenous skeletal muscle TFEB expression is maintained
217 across the lifespan of our cTFEB;HSACre model (**Figure 1B**).

To visualize the key networks of differentially expressed proteins associated with TFEB-overexpression, we performed a functional enrichment analysis on all overexpressed proteins using the STRING protein-protein interaction network [42] (**Figure 2C**). Using TFEB as our 'bait' for functional connectivity nodes, we identified two clear interaction networks: the first one was associated with lysosomal biogenesis and function (**Figure 2C, blue**), and included Lamp1 (an essential lysosomal structural protein), Grn (progranulin) and Psap (prosaposin) as well as the lysosomal proteases: Ctsb (Cathepsin B), Ctsd (Cathepsin D), and Ctsl (Cathepsin L). The second interaction network is associated with key skeletal muscle proteostasis and metabolic signaling pathways including mTOR, Akt and GSK3β (**Figure 2C, green**). Both of these nodes are key elements of the signaling network controlled by TFEB-mediated transcription [31,32], were previously reported to be transcriptionally elevated in skeletal muscle after viral-mediated TFEB overexpression [36], and are central regulators of aging [1].

To further understand the functions of all the upregulated proteins in TFEB-overexpressing skeletal muscle, KEGG enrichment analysis was performed. As expected, central proteostasis categories were significantly upregulated in young TFEB-overexpressing skeletal muscle: including Hypoxia-inducible factor 1 (HIF-1) signaling, proteasome, and autophagy/lysosomal function categories (**Figure 2D, orange**). Importantly, this enrichment in proteostasis categories and TFEB-regulated nodes of signaling was also present in our aging cohorts (**Figure 2D, top**). We confirmed functional activation of TFEB-dependent transcription in cTFEB:HSA-Cre bigenic muscle, using our previously reported TFEB-responsive muscle gene targets [27] including *Lamp1*, *Atg5* (a key regulator of autophagy initiation), *Ctsd* and *Ctsb* (**Figure 2E**). Immunoblotting studies confirmed significant increases in Lamp1 and Ctsd protein in cTFEB;HSACre bigenic muscle (**Figure 2F**). Consistent with previous studies demonstrating TFEB overexpression increases the number and size of LAMP1-positive lysosomes in multiple tissues [30,35,43], we also detected significant increases in the number of LAMP1+ puncta and total LAMP1+ area in cross-sections of young female (and similar trends in male) cTFEB;HSACre skeletal muscle (**Figure 2G**). There were no significant changes to LC3II/LCI ratios or total polyubiquitinated protein levels in cTFEB;HSACre transgenic mice (**Supplemental Figure 2I**). These findings confirm physiologically significant increases in TFEB-dependent transcription [36] and lysosomal biogenesis [32,36] in skeletal muscle of cTFEB:HSA-Cre mice.

Additional functional categories enriched in our proteomics analysis related to cellular metabolism and mitochondrial function, including thermogenesis, oxidative phosphorylation and pyruvate metabolism (**Figure 2D, gold**). We also detected central fatty acid metabolism

251 pathways, including PPAR signaling and metabolism, and degradation and biosynthesis of fatty
252 acids (**Figure 2D, green**). This is consistent with previously published reports suggesting that
253 acute TFEB expression in young skeletal muscle induces the expression of genes involved in
254 mitochondrial biogenesis and oxidative phosphorylation [36]. Here we confirm for the first time that
255 these changes in cTFEB;HSACre muscle are maintained throughout aging, particularly those
256 associated with mitochondrial metabolism and fatty acid metabolism (**Figure 2D, top, gold and**
257 **green**).

258 We assessed whether these proteomic profiles associated with mitochondrial function translated
259 into mitochondrial function differences using high-resolution respirometry with simultaneous
260 measurements ROS production assays [44]. As reported previously for soleus skeletal muscle [44],
261 oxygen consumption rates decrease with aging across all mitochondrial complexes in semi-
262 permeabilized soleus muscle of control mice of both sexes (6 vs. 18 months of age, gold icons)
263 (**Figure 2H-2I**). Whereas there was no difference in mitochondrial respiration rates between
264 control and TFEB-overexpressing skeletal muscle at young ages (closed icons), respiration
265 rates of aged cTFEB;HSACre transgenic muscle (open icons) remained comparable to their
266 young counterparts across all mitochondrial complexes examined (**Figure2 H-2I**), particularly in
267 female muscle. Together with our functional data showing increases in exercise capacity in
268 cTFEB;HSACre mice (**Figure 1L-M**), these results suggest that muscle-TFEB overexpression
269 promotes maintenance of mitochondrial function and bioenergetic reserves, preventing the age-
270 associated decline of mitochondrial respiration commonly observed in aging skeletal muscle [1,44].

271 Finally, proteomics KEGG analysis also showed enrichment in cTFEB;HSACre bigenic muscle
272 for classical signaling pathways shown to decline during aging, including the Insulin-IGF1-
273 signaling (IIS) and AMPK signaling [1] (**Figure 2D, blue**). We also detected multiple hits for
274 amino acid metabolism pathways, such as catabolism of branched-chain amino acids (BCAAs),
275 including valine, leucine and isoleucine metabolism (**Figure 2D, purple**). Importantly, these
276 changes were still evident in our aged cohorts (**Figure 2D, top**), consistent with our functional
277 studies suggesting that TFEB overexpression throughout the lifespan has multiple benefits in
278 skeletal muscle, targeting established hallmarks of aging [1].

279 The skeletal muscle 'secretome' (the totality of released organic and inorganic molecules
280 released from muscle resident cells) is highly dynamic, responding to physiological and
281 pathophysiological stimuli [45,46] and potentially also changing with age [46]. To directly examine any
282 changes to the skeletal muscle protein-based secretome associated with TFEB-overexpression,

283 we pursued additional *in silico* analysis through the Vertebrate Secretome Database (VerSeDa)
284 on our proteomics cohorts to identify unique age- and genotype-associated signatures of
285 potentially secreted proteins [47] differentially expressed in cTFEB;HSACre skeletal muscle. We
286 identified multiple proteins with predicted secreted profiles to be enriched in young and aged
287 TFEB-expressing skeletal muscle (**Figure 3A**). Some secreted proteins exhibited upregulation
288 (e.g., nucleobindin-1, angiopoietin-related protein 1) or down-regulation (collagen alpha-1 (I)
289 chain), only in young cTFEB;HSACre muscle (**Figure 3A, green**). Others remained up-
290 regulated at both ages in cTFEB;HSACre muscle, (prosaposin, mammalian ependymin-related
291 protein 1 (MERP1) and dehydrogenase/ reductase SDR family member 7C, D/R SDR7C)
292 (**Figure 3A, overlap**), or were only differentially expressed in aged muscle (biglycan-1, PG-S1,
293 **Figure 3A, blue**), highlighting the dynamic nature of the skeletal muscle secretome throughout
294 aging. Cathepsin B (Ctsb), a previously documented muscle-originating secreted factor with
295 known CNS-targeting effects [20] and a known target of TFEB-dependent transcription (**Figure**
296 **2E**) [32] was our top up-regulated hit at both ages examined. We validated significant increases in
297 pro-enzyme levels of Ctsb in both sexes and at both ages examined (**Figure 3B**), as well as
298 significant increases in mature (secreted) Ctsb isoforms in aged cTFEB;HSACre transgenic
299 muscle (**Figure 3B**). We also detected trends towards increased levels of circulating CTSB in
300 the serum of female cTFEB;HSACre mice (**Figure 3E**). Given the potent remodeling of the
301 lysosomal network associated with activation of TFEB-mediated transcription (**Figure 2**) [30-32],
302 our data suggests that overexpression of TFEB in skeletal muscle drives increased expression
303 and secretion of mature Ctsb, a CNS targeting-factor, into circulation.

304 **Enhanced skeletal muscle TFEB-signaling reduces accumulation of**
305 **hyperphosphorylated tau and microglial activation in a mouse model of tau pathology.**

306 To assess any potential neuroprotective effects of enhancing skeletal muscle TFEB-signaling in
307 the context of age-associated neurodegenerative disease pathologies, we derived
308 cTFEB;HSACre transgenic mice on the MAPT P301S (PS19) background. This is a well-known
309 model of neurofibrillary tangle toxicity, a hallmark of AD and related tauopathies [48], and is
310 characterized by prominent accumulation of hippocampal hyperphosphorylated human mutant
311 MAPT protein and pronounced neuroinflammation, including microgliosis and astrocyte
312 reactivity [48].

313 We first confirmed muscle-restricted 3x-FLAG-TFEB overexpression in skeletal muscle lysates
314 from MAPT P301S;cTFEB;HSACre mice, as well as the presence of human Tau in hippocampal

315 lysates of both groups via immunoblotting (**Figure 4A**). As previously reported [48], at 9 months of
316 age there is robust accumulation of Ser202/Thr205 hyperphosphorylated tau (residues
317 abnormally phosphorylated in paired helical filaments during AD progression) in the dentate
318 gyrus of the hippocampus of MAPT P301S mice of both sexes [48] (**Figure 4B, middle panel**).
319 Conversely, we noted a significant reduction in the total fluorescence counts of AT8-positive
320 phosphorylated tau in the dentate gyrus of MAPT P301S;cTFEB;HSACre mice (**Figure 4B**,
321 **purple**) compared with MAPT P301S littermate controls (**Figure 4B**, **teal**). More so, this
322 reduction was particularly evident in the levels of 'intracellular tau' accumulating around
323 hippocampal cell bodies (**Figure 4B, insets**), suggesting reduced accumulation of toxic tau
324 species and aggregates [49] in the hippocampus of MAPT P301S;cTFEB;HSACre mice. We
325 confirmed similar but less striking reductions in Thr231 phospho-tau (another primary site of tau
326 phosphorylation associated with neurotoxic tau accumulation) immunostaining (**Supplemental**
327 **Figure 3A**), suggesting overall reductions in tau hyperphosphorylation in the hippocampus of
328 MAPT P301S transgenic mice with TFEB overexpression in skeletal muscle.

329 Astrocytes and microglia are key mediators of neuroinflammation, and undergo key
330 morphological and functional alterations during neurodegenerative disease, including changes
331 in ramification and cellular process complexity [50], reduced immune surveillance activity [51] and
332 increased reactivity phenotypes [52]. We confirmed significant increases in the staining for GFAP-
333 positive structures (a marker of astrocyte reactivity) in the dentate gyrus of 9-month-old MAPT
334 P301S mice of both sexes (**Figure 4C, teal**) compared to their MAPT-negative littermate
335 controls (**Figure 4C, gold**). We also detected significant increases in the volume of IBA1+-
336 positive microglia in the same brain region (**Figure 4C, teal**), consistent with previous reports in
337 the MAPT P301S model indicating high levels of neuroinflammation starting as early as 4
338 months of age [48,53]. Strikingly, we noted significant reductions in both of these pro-inflammatory
339 glial morphometric parameters in the hippocampus of MAPT P301S;cTFEB;HSACre littermates
340 (**Figure 4C, purple**), suggesting overall reduced hippocampal neuroinflammation during
341 symptomatic disease stages through activation of skeletal muscle TFEB-expression.

342 **Enhancing TFEB-signaling in skeletal muscle promotes neurotrophic signaling and**
343 **reduces hippocampal neuroinflammation in MAPT P301S transgenic mice**.

344 To gain more precise insights into disease-relevant transcriptional changes in the hippocampus
345 of MAPT P301S mice with enhanced muscle-TFEB expression, we used the Nanostring
346 nCounter® Mouse Alzheimer's Disease panel. This platform directly assesses the expression of

347 770 targeted genes curated from human and pre-clinical models of AD and robustly captures
348 disease-relevant signatures and their modifications after pre-clinical interventions [54]. Using this
349 approach, we found 24 individual differentially expressed genes in MAPT
350 P301S;cTFEB;HSACre hippocampi compared to their littermate MAPT P301S+ controls
351 between both sexes (**Supplemental Figure 3B-C**). Interestingly, most differentially regulated
352 genes were downregulated (18 of 24), consistent with their identity as transcriptional drivers of
353 disease [54]. Many of these transcripts are associated with microglial activation (*Rhoc, Clic1)*
354 markers of neuronal function (*Gdap1l1, Amot, Map3k9),* phospholipid and cholesterol
355 remodeling (*Ano6, Cyp27a1*), growth factor signaling (*Vgf*), endothelial cell migration and matrix
356 adhesion (*Rras, Cdc42Ep1*) and guanine nucleotide exchange factors (*Dock3*). Multiple down-
357 regulated genes were associated with novel variants and loci associated with increased
358 polygenic neurodegenerative disease risk (*Prkd3, Arhgap31)* as well as predictors of the rate of
359 cognitive decline in AD (*Hecw1* [55]). *Pbxip1,* another significantly downregulated marker, has
360 been found to be associated with phosphorylated-tau and $A\beta_{1-40}$ levels in the human temporal
361 cortex[56]. Additional transcriptional changes of significance include genes of unknown function
362 but are classified as transcriptional identifiers of AD progression *(Ptprn, Cpne2,* and *Eri2)*[54]. Up-
363 regulated transcripts included gene repressors (*Zbtb33*), modulators of neuroinflammation
364 (*Pecam1*) and neurodegeneration (*Scna*), as well as a carbohydrate transmembrane transporter
365 (*Tmem144*) and a GTP-ase nucleotide exchange factor (*Rcc1*).

366 Annotation of the differentially co-expressed/co-functional clusters included in this panel
367 revealed significant reductions in the nCounter AD microglial activation module (composed of 63
368 genes associated with microglial activation during AD progression) (**Figure 4D**) in the
369 hippocampi of 6 month old female (but not male) MAPT P301S;cTFEB;HSACre mice compared
370 with MAPT P301S littermates. This is consistent with reduced neuroinflammation in the
371 hippocampus of MAPT P301S mice with enhanced muscle-TFEB expression, as suggested by
372 our glial morphometric analysis (**Figure 4C**). Interestingly, we also detected a sex-bias in the
373 trophic factor functional cluster (composed of genes *Arhgdib, Bcl2, Calm3, Camk4, Gab1,*
374 *Mapk9, Mapkapk2, Ntrk2, Pik3r1* and *Psen1*), with a significant improvement back to baseline
375 expression in the hippocampus of male (but not female) MAPT P301S;cTFEB;HSACre mice
376 (**Figure 4E**). We confirmed activation of neurotrophic signaling as early as 6 months of age in
377 the hippocampus of male MAPT P301S;cTFEB;HSACre mice by targeted qRT-PCR analysis,
378 which showed corrections of declining expression levels of neurotrophic factors *Bdnf* and *Fndc5*
379 back to control littermate levels (**Figure 4F-G**) [23,57]. Importantly, there was also a significant

extension (38%) in the lifespan of male MAPT P301S;cTFEB;HSACre mice (**Figure 4H**). While the median survival of male MAPT P301S mice was 352 days (**Figure 4H, teal curve**), male MAPT P301S;cTFEB;HSACre mice median survival was 489 days (**Figure 4H, purple curve).** Although we did not detect a similar lifespan extension in female MAPT P301S;cTFEB;HSACre mice (**Figure 4I**), it is worth noting that in our hands, female MAPT P301S transgenic mice already live significantly longer than their male littermate controls (median survival of 468.5 days), perhaps suggesting they have reached maximal lifespan in this model. Finally, we did not detect any differences in ataxia progression [58] (**Supplemental Figure 3D**) or weight loss (**Supplemental Figure 3E**) between our groups. Altogether, these provocative results suggest that enhanced skeletal muscle-TFEB expression modifies the accumulation of pathogenic tau isoforms, reduces neuroinflammation and re-activates neurotrophic signaling in the hippocampus of MAPT P301S mice in a sex-dependent manner. Importantly, this occurs in the absence of detectable exogenous human TFEB expression in the CNS (**Supplemental Figure 1**), suggesting an independent mechanism of muscle-to-brain communication underlying these effects.

Skeletal muscle over-expression of TFEB decreases neuroinflammation markers and lipofuscin accumulation in the healthy aged CNS.

To examine the effect of increased muscle-TFEB expression on the healthy aging brain without neurodegenerative disease burden, we assessed the transcriptional and functional status of known inflammatory markers in the CNS of healthy aged (20+ months old) control and cTFEB;HSACre mice, an age when global decreases in proteostasis and increases in pro-inflammatory signaling are detectable in most murine tissues [1,59], including the CNS [1,2]. Total hippocampal mRNA levels of *Ccl2* and *Nfκb*, pro-inflammatory cytokines previously reported to mediate microglial responses to inflammation, were significantly reduced in the hippocampus of aging female (but not male) cTFEB;HSACre bigenic mice (**Figure 5A-B**). Interestingly, the expression of *Il6* (interleukin 6) was significantly elevated in the same groups (**Figure 5C**). We also detected significantly higher levels of expression of *Bdnf* (Brain Derived Neurotrophic Factor) in hippocampal lysates from aged male (but not female) mice (**Figure 5D**), similar to the upregulation of hippocampal BDNF we observed in our male MAPT P301;cTFEB;HSACre model (**Figure 4F**).

Using similar morphometric analysis as before to quantify glial cell shape and morphology, we did not detect any differences in microglia (IBA1+) or astrocyte (GFAP+) number, volume or

412 ramification state in the dentate gyrus of aged cTFEB;HSACre bigenic mice compared to their
413 littermate controls (**Figure 5E-F**). This may suggest that the expression differences observed
414 via transcriptional approaches above may either originate in non-glial cells (neurons or
415 endothelial cells, for example) or not translate into detectable morphological changes at the
416 ages examined. It is important to note that age-associated changes in neuroinflammation in an
417 otherwise healthy brain are not as pronounced as those seen in the context of
418 neurodegenerative disease (such as in the MAPT P301S model, for example). Overall, these
419 results suggest a shift in the cytokine transcriptional landscape of the aging female
420 hippocampus with upregulated skeletal muscle TFEB-expression towards reduced inflammatory
421 signaling, consistent with what we observed in our MAPT P301S studies (**Figure 4**).

422 Accumulation of lipofuscin, a non-degradable intracellular auto-fluorescent polymer, becomes
423 prominent in the aging brain, likely reflecting an age-associated decline in basal CNS autophagy
424 [1]. We examined the clearance capabilities of the aging CNS by indirect immunofluorescence of
425 lipofuscin granules in brain sections of aged (21-24 months old) control and
426 cTFEB;HSACre mice. While we detected striking lipofuscin granule accumulation in several
427 brain regions of aged control mice, including the hippocampus (**Figure 5G, top**), there was a
428 significant decrease in lipofuscin deposition in the dentate gyrus of aged
429 cTFEB;HSACre females (**Figure 5G, bottom),** with a similar non-significant trend in males. To
430 determine any changes in proteostasis associated signaling in this brain region, we next
431 examined the transcriptional levels of multiple autophagy and lysosomal associated genes.
432 Consistent with previous reports, we confirmed significant age-associated increases in the
433 expression of autophagy lysosomal markers *Atg8/Lc3*, *Lamp1, Sqstm1,* and *Ctsd* in the male
434 hippocampus, which has been proposed to occur as a compensation for age-associated decline
435 in proteostasis function (**Figure 5H-K**). Interestingly, these differences were not as prominent in
436 the aging control female hippocampus. Furthermore, some of these transcriptional increases
437 were reduced in the hippocampus of aged male cTFEB;HSACre bigenic mice, suggesting that
438 enhancing skeletal muscle TFEB-signaling promotes maintenance of hippocampal proteostasis
439 during aging. Our data thus indicate a potential sex-bias in activation of neuroprotective
440 signaling in the hippocampus of aging cTFEB:HSACre bigenic mice, with females showing
441 decreased neuroinflammation (**Figure 5A-C**) and males showing increased neurotrophin
442 expression levels (**Figure 5D**). Altogether, our results suggest that overexpression of TFEB in
443 skeletal muscle throughout the lifespan promotes maintenance of protein quality control

regulation in the CNS, ultimately reducing proteostatic burden and neuroinflammation in the aging hippocampus, similar to what we observed in our MAPT P301S studies.

Improved performance in neurocognitive testing of aging cTFEB;HSACre mice.

We next pursued neurocognitive testing in aged (16-18 months old) control and cTFEB;HSACre mice. First, we evaluated spatial learning and memory using the Barnes maze task, a hippocampal working memory test known to be sensitive to aging in mice. We documented a significant decrease in the number of errors per trial (**Figure 5L**) and significantly faster escape times (**Figure 5M**) in aged cTFEB;HSACre mice of both sexes in comparison to controls. By the last trial, cTFEB;HSACre mice escaped the maze twice as quickly as control mice. In the novel object recognition task – an independent behavioral test of hippocampal recognition memory – we also found that aged cTFEB;HSACre mice of both sexes exhibited a significantly greater number of contacts with the novel object compared to controls during the test phase (**Figure 5N**). Indeed, aged cTFEB;HSACre mice have around a ~15% higher preference for the novel object relative to their age-matched littermate controls (**Figure 5O**). Importantly, we also confirmed no differences in visual performance and motor activity (not shown) between aged control and cTFEB;HSACre cohorts. Hence, these results provide exciting evidence for a pronounced improvement in neural function in the aging brain of cTFEB;HSACre mice.

Enhancing skeletal muscle TFEB-signaling transcriptionally remodels the hippocampus of cTFEB;HSACre bigenic mice throughout the lifespan in a sex-dependent manner.

To determine the molecular basis of the benefits of enhancing skeletal muscle TFEB-signaling on the aging CNS, we performed unbiased transcriptome analysis on hippocampal RNAs isolated from young (6 months old) and aged (22-24 months old) mice (**Figures 6-7**). By this time point, aging control animals have increased neuroinflammation (**Figure 5A-B**), have evident CNS proteostasis dysfunction (**Figure 5G**), and display deficits in cognitive function (**Figure 5L-O**), phenotypes that are significantly improved in cTFEB;HSACre mice.

Bulk RNA-Seq analysis of hippocampal RNA lysates revealed robust changes in gene expression in young cTFEB;HSACre bigenic mice compared to their age- and sex-matched littermate controls (**Figure 6, Figure 7, Supplemental Figure 4, and Supplemental Figure 5**). In young female cTFEB;HSACre hippocampi, we detected 618 differentially expressed genes,

474 (DEGs, 435 up-regulated and 165 down-regulated) (**Figure 6A**). Functional GO Enrichment
475 analysis showed these DEGs mapped to key categories associated with synaptic function,
476 including ion- and voltage-gated channel activity, transporter complexes, as well as synapse
477 and synaptic membrane categories (**Figure 6C, boxes**). Enrichment analysis of differential
478 gene expression (KEGG) revealed additional critical categories associated with neural function,
479 including oxytocin signaling, cAMP signaling, Hippo signaling and gap junctions (**Figure 6E**).
480 Furthermore, metabolic and functional pathway analysis (Reactome) also identified key
481 categories known to regulate cognitive plasticity, including GPCR ligand binding, voltage gated
482 potassium channels, and transmission across chemical synapses, among others
483 (**Supplemental Figure 4A**).

484 Consistent with our biochemical and functional findings suggesting increased neuroprotective
485 benefits in aging cTFEB;HSACre mice (**Figure 5**), we found that these transcriptional changes
486 modulating synaptic function pathways are still present (although not as prominent) in the aging
487 hippocampus of aged female cTFEB;HSACre mice (**Figure 6B, Supplemental Figure 4B&D**).
488 Out of a total of 1765 DEGs, (541 up-regulated and 1224 down-regulated), KEGG functional
489 pathways enriched in our aged female hippocampus included key categories associated with
490 preservation of neuronal activity and cognitive function, including axon guidance, HIF-1
491 signaling, AMPK signaling and PI3-Akt signaling (**Figure 6F**). We confirmed the age-associated
492 differential expression of a subset of our top-hit genes in a second group of hippocampal RNA
493 lysates using targeted qRT-PCR (**Supplemental Figure 4E**). Altogether, this suggests that
494 overexpression of TFEB in skeletal muscle activates multiple neuroprotective gene networks
495 associated with synaptic function and signaling in the young and aged female hippocampus.

496 Conversely, in the young male cTFEB;HSACre hippocampus mice we detected 471 DEGs with
497 a 1.25-fold expression change (216 up-regulated and 255 down-regulated), which GO-term
498 analysis associated mostly with multiple mitochondria or ribosomal/transcription targeting
499 pathways (**Figure 7A and C, boxes**). This included mitochondrial respiratory chain,
500 mitochondrial protein complexes, electron transport chain and ATP metabolic processes
501 (**Figure 7C**). Additional enriched metabolic pathways in the hippocampus of young
502 cTFEB;HSACre males included non-sense mediated decay, metabolism of RNA and translation
503 (**Supplemental Figure 5A**). Consistent with this, KEGG analysis revealed the most enriched
504 functional pathways were ribosomes and oxidative phosphorylation (**Figure 7E**). As before, we
505 confirmed the differential expression of a random sampling of our top-hit genes using targeted

506 qRT-PCR (**Supplemental Figure 5E).** When we performed similar analysis on the male aging
507 hippocampus, we detected 539 DEGs in the hippocampus of aged male cTFEB;HSACre mice
508 (278 up-regulated, 261 down-regulated) (**Figure 7B**), with only mild significance on functional
509 pathways (**Figure 7D, Figure 7F, Supplemental Figure 5B, and Supplemental Figure 5D**).

510 Further analysis also revealed that most DEGs appeared to be sex-specific. Out of all DEGs in
511 young cTFEB;HSACre hippocampi (618 in females and 471 in males), there were only 25
512 shared DEGs, with 16 of these changing in the same direction in both sexes (**Supplemental**
513 **Figure 6A**). A similar pattern was found in the aged cTFEB;HSACre hippocampus (1765 total
514 DEGs in females and 539 DEGs in males), with 39 shared DEGs and only 3 genes changing in
515 the same direction in both sexes (**Supplemental Figure 6B**). Our results thus strongly suggest
516 a sex bias in the hippocampal transcriptional responses associated with muscle-TFEB
517 overexpression, with the female hippocampi up-regulating neuronal signaling and synaptic
518 function and the male hippocampi upregulating transcriptional and mitochondrial responses.
519 Finally, many of these changes are preserved up until late stages in the lifespan of our model
520 (24 months of age), suggesting that these transcriptional changes may underlie the
521 neurocognitive benefits observed in our aging cTFEB;HSACre cohorts.

522 **DISCUSSION**

523 Skeletal muscle comprises roughly 40% of the total body mass in a healthy young adult human
524 and is highly susceptible to age-associated metabolic and functional decline [60,61]. Skeletal
525 muscle health has recently been linked to multiple chronic age-associated conditions, including
526 neurodegenerative diseases [24,26], but the role of the so-called muscle-to-brain axis on the
527 pathology of these conditions remains largely unknown. Here, and for the first time in mammals,
528 we provide direct evidence demonstrating the CNS benefits of enhancing muscle-TFEB
529 expression, both during healthy aging and in the context of neurodegenerative proteinopathy.

530 We found that lifelong overexpression of TFEB, a master regulator of lysosomal and
531 mitochondrial function, reduces age-associated functional and biochemical hallmarks of aging in
532 skeletal muscle [1] **(Figure 1-2)**. We confirmed previous reports showing that in young skeletal
533 muscle, acute TFEB-overexpression induces the expression of genes involved in mitochondrial
534 biogenesis, fatty acid oxidation, and oxidative phosphorylation, optimizing mitochondrial
535 substrate utilization and enhancing exercise capacity [36]. Furthermore, we extend these findings
536 and report that life-long overexpression of muscle-TFEB counteracts age-associated

537 mitochondrial dysfunction in skeletal muscle (**Figure 2**) [1,44], ultimately preserving skeletal
538 muscle mass and preventing fiber type switching during aging (**Figure 1**). Indeed, young TFEB-
539 overexpressing muscle had significant increases in the abundance of Type 1 and Type 2A
540 fibers, which are considered to be highly reliant on oxidative phosphorylation and thus more
541 resistant to fatigue. This is consistent with the observed increases in exercise performance of
542 cTFEB;HSACre transgenic mice at both ages (**Figure 1**). Importantly, although we focused our
543 analysis on two key hallmarks of aging (lysosomal and mitochondrial function), our proteomics
544 studies also detected important changes in branched chain amino acid signaling, which have
545 been recently linked to lifespan and healthspan extension in rodents [62], indicating that TFEB
546 overexpression may have pan-geroprotective effects on aging skeletal muscle.

547 The hippocampus is a critical structure in cognitive aging, and hippocampal atrophy and
548 dysfunction are key features of both aging and neurodegenerative diseases [63,64]. In addition to
549 rescuing age-associated hallmarks in skeletal muscle, we also discovered significant
550 improvements in multiple disease-associated biochemical hallmarks in the hippocampus of
551 cTFEB;HSACre transgenic mice. Indeed, we observed robust benefits on morphological and
552 transcriptional markers of neuroinflammation in the MAPT P301S model of tau toxicity, as well
553 as a significant extension on the lifespan of male MAPT P301S;cTFEB;HSACre transgenic mice
554 (**Figure 4**). We also report important reductions in proteotoxicity and neuroinflammation and
555 improved neurocognitive performance in healthy aging (22-24 month old) cTFEB;HSACre mice
556 (**Figure 5**). Importantly, we observed these benefits without any detectable expression of our
557 transgene in the CNS (**Supplemental Figure 1**). Although previous work examining the muscle-
558 to-brain axis has demonstrated important benefits on the accumulation of misfolded protein
559 inclusions in the CNS [5,8,19,28], similar to what we observed in the MAPT P301S;cTFEB;HSACre
560 hippocampus, the profound reductions in neuroinflammation observed in our model suggest
561 modulation of skeletal muscle TFEB-signaling may be a novel target to modulate
562 neuroinflammatory signaling in vivo in the context of aging and/or neurodegenerative diseases.

563 Previous transcriptional studies of the healthy aging hippocampus have identified dysregulation
564 of ion homeostasis, disruption of neurotransmission, and ribosome biogenesis as key biological
565 process exhibiting differential regulation with aging [2,65]. Specifically, genes related to synaptic
566 transmission and plasticity appear to be particularly sensitive to age-associated transcriptional
567 dysregulation (reviewed here [3]). Many of these gene networks are also significantly altered in
568 AD and other associated tauopathies [57]. It was quite interesting that similar networks were
569 transcriptionally remodeled in the healthy aging cTFEB;HSACre hippocampus, suggesting that

570 these gene networks may be uniquely sensitive to both neurotoxic (aging, neurodegeneration)
571 and neurotrophic (muscle-TFEB overexpression) signaling. Indeed, manipulation of skeletal
572 muscle TFEB modulated expression of similar functional enrichment categories (i.e. trophic
573 factor signaling, neuroinflammation) in the aging and tau-afflicted hippocampus of our
574 cTFEB;HSACre mice in a sex-dependent manner. When we compared KEGG pathways of the
575 differentially expressed genes from the nCounter AD panel in MAPT P301S;cTFEB;HSACre
576 hippocampus with those enriched in the hippocampus of our 24-month old cTFEB;HSAcre mice,
577 we see shared regulation of pathways involved in axon guidance, MAPK signaling, cAMP
578 signaling, and Neuroactive ligand-receptor interactions, suggesting potential converging
579 neurotrophic benefits associated with muscle-TFEB expression.

580 One of our most exciting (and unexpected) findings is the sex-bias in our CNS and skeletal
581 muscle responses to muscle-TFEB overexpression. In general, we struggled to identify previous
582 literature thoroughly describing female-specific changes to many of these hallmarks of aging on
583 either tissue [1]. To our surprise, while we were able to validate 'classical' age-associated findings
584 such as fiber type switching in aging control males, these phenotypes were less robust or not
585 present in age-matched control females (**Figure 1**), rendering interpretation of the sex-bias of
586 our CNS-targeting benefits difficult. While we ultimately observed neuroprotective effects on
587 both male and female cTFEB;HSACre transgenic mice, it appears that the mechanisms
588 underlying these benefits are not the same. For example, whereas muscle-TFEB
589 overexpression in the MAPT P301S model reduces the accumulation of hyperphosphorylated
590 tau in both sexes, it appears to drive the transcriptional silencing of pro-inflammatory microglial
591 signaling in females, and activate trophic factor signaling in males instead. We also detected
592 similar sex-differences in our healthy aging transcriptional studies, with the female
593 cTFEB;HSACre hippocampus activating pathways associated with synaptic function, while the
594 male cTFEB;HSACre hippocampus activated ribosomal and mitochondrial signaling instead.
595 One potential explanation could be the sex-bias in TFEB expression in skeletal muscle, which is
596 ~50% higher in male mice, suggesting a threshold effect for local remodeling of skeletal muscle.
597 However, the fact both sexes do display similar exercise endurance at young ages and
598 comparable protection of mitochondrial respiration rates at old ages again suggest converging
599 outcomes of TFEB-mediated geroprotection of aging skeletal muscle. Another consideration is
600 that in our healthy aging studies, both sexes are well into the stage of reproductive senescence,
601 which has been reported to have significant negative impacts on neural function [66]. While we did
602 not measure circulating levels of sex hormones in our models, there is plenty of evidence for de

603 novo synthesis on neuroactive steroids in the brain having neurotrophic and anti-inflammatory
604 benefits, the phenotypes we also see being modified in our cTFEB;HSACre groups.
605 Interestingly, CNS estrogen appears to control similar signaling pathways as those we detected
606 as differentially expressed in the hippocampus of muscle-TFEB overexpressing female (i.e.
607 synapse function, neurotransmitter signaling) and male (i.e. mitochondrial function) mice [66].
608 While it is unclear whether these differential responses between male and female hippocampi
609 reflect local differences in the CNS itself (as recently published here [67]) or peripheral differences
610 in the expression, secretion or trafficking of circulating signals (such as Ctsb, for example), they
611 underscore the fundamental need to examine sex differences contributing to the biology of
612 aging and neurodegenerative diseases [68].

613 Recent evidence has shown that muscle-originating circulating factors (myokines) appear to
614 play central roles in regulating CNS health and function. Ctsb is secreted from skeletal muscle
615 into circulation in response to exercise, and is required for the full manifestation of exercise-
616 associated benefits on the CNS, including increases in hippocampal Bdnf and the activation of
617 neurogenesis [20]. Circulating Ctsb has also been proposed to cross the blood-brain barrier [20],
618 and appears to remodel the extracellular matrix [69] , enhancing axonal outgrowth through
619 degradation of chondroitin sulfate [70,71]. Furthermore, high Ctsb expression levels in the
620 hippocampus have been reported in low-anxiety mouse lines [72,73], suggesting that Ctsb may
621 play important roles in maintaining neuronal homeostasis in brain regions with high relevance
622 for both aging and age-associated neurodegenerative disease. Through our proteomics in silico
623 analysis, we identified Ctsb as our highest expressed secreted factor in cTFEB;HSACre skeletal
624 muscle, and we confirmed higher levels of circulating Ctsb in the serum of cTFEB;HSACre
625 transgenic mice. Our results imply that additional research into the role and function of
626 circulating proteases and their ability to remodel the CNS may be warranted. Interestingly,
627 recent evidence demonstrates pronounced involvement of the (macro)autophagy molecular
628 machinery in cellular secretion [74]. Indeed, key signaling molecules and cytokines associated
629 with inflammation, such as IL1B (interleukin 1 beta) and IL6 (interleukin 6), are released into the
630 extracellular space via autophagy-dependent secretion. There is also a growing body of
631 evidence that age [46] and exercise [75], known modifiers of skeletal muscle metabolism, alter the
632 composition of the skeletal muscle secretome. This suggests that activation of TFEB-
633 overexpression may be modifying the skeletal muscle secretome, potentially enriching it with
634 neurotrophic factors or depleting it from neurotoxic factors, although this hypothesis remains to
635 be tested.

636 Over the last ten years, there has been growing evidence that suggests prominent contributions
637 of the periphery to the etiology of neurodegenerative diseases. Our discovery that skeletal
638 muscle TFEB-signaling can be a crucial site for regulation of CNS health and function provides
639 compelling evidence for a new therapeutic delivery avenue into the brain, providing a currently
640 unexplored new diagnostic and therapeutic intervention site (i.e. skeletal muscle) for preserving
641 brain health.

642 **Authorship Contributions**

643 IM, CJC, AG, HM, AB, AH, KL, EL, KC, MM, DP, MB, AN, NN, GM, LW, MM, NM, EB and EF:
644 Performed the experimental work. Reviewed and edited the manuscript.

645 CJC and IM: Wrote and edited the manuscript.

646 CJC and ALS: Conceptualized the experiments outlined here and obtained all associated
647 funding.

Figure Legends

Figure 1: Skeletal muscle overexpression of TFEB preserves muscle size, fiber typing and increases exercise endurance during aging.

(A) Schematic depicting 3x-FLAG human TFEB transgene. Cassettes are arranged from 5' (left) to 3' (right). Note that the 3x-FLAG-EGFP-STOP cassette (flanked by loxP sites) prevents expression of the 3x-FLAG human TFEB transgene unless in the presence of Cre recombinase.

(B) Immunoblot of control and cTFEB;HSACre quadriceps lysates confirming 3x-FLAG-TFEB protein expression in young (5-6 months) and aged (22-24 months) mice of both sexes. C=control, T=cTFEB;HSACre individuals. Transgenic 3x-FLAG-TFEB protein weighs ~75 kDa. Total Protein Stain Free lanes are shown below as a loading control. Densitometry quantification relative to average of young male control individuals to the right.

(C-E) Skeletal muscle (quadriceps, C and gastrocnemius, D) wet weight and body weight (E) in young (6 months) and aged (22-24 months) control and cTFEB;HSACre transgenic mice of both sexes.

(F) Representative images of fibertyping stains of cross-section of gastrocnemius muscle of young (7-9 months) and aged (22-24 months) control and cTFEB;HSACre transgenic mice of both sexes. MyHC1 (Fiber Type 1) in red, MyHC2A (Fiber Type 2A) in green, MyHC2B (Fiber Type 2B) in blue, MyHC2X (Fiber Type 2x) unstained, and laminin in white. Scale bars = 500 μm.

(G) Fiber cross sectional area distribution curves from (F). *, statistical difference between control and cTFEB;HSACre. #, statistical difference between young and aged controls. Each data point represents the average of 3 separate images collected from 3 sections/individual.

(H-K) Quantifications of each fiber type percentage from (F). Each data point represents the average of 3 separate images collected from 3 sections/individual.

(L-M) High-intensity exhaustive treadmill exercise of young (6 months) and aged (18 months) control and cTFEB;HSACre transgenic mice of both sexes showing maximum distance run till exhaustion (L) and total work (body weight/distance run, M).

Each point represents the average of all data from a single individual. Controls are age-matched littermates. Unless otherwise stated, data are presented as mean ± SEM. */# $p<0.05$, **/## $p<0.01$, ****/#### $p<0.0001$ ANOVA and post-hoc multiple comparisons for each sex. Lack of annotation indicates comparisons were not significant.

Figure 2: Muscle TFEB increases lysosomal network size and preserves mitochondrial function during aging.

(A-B) Volcano plot of proteomics analysis depicting differentially regulated proteins in young (A, 6 months old) and aged (B, 18 months old) cTFEB;HSACre quadriceps muscle relative to controls. Overexpressed proteins in red, underexpressed proteins in blue. TFEB (rectangles) is highly expressed in both aged and young muscle.

(C) STRING predicted protein-protein interactions of overexpressed proteins from (A) showing interacting networks converging on TFEB (blue) and mTOR (green).

(D) KEGG enrichment analysis clusters overexpressed proteins from (A-B) into categories associated with proteostasis and autophagy (orange), mitochondrial metabolism (gold), fatty acid metabolism (green), age-associated signaling (blue), and amino acid metabolism (purple).

(E) qRT-PCR for *Lamp1*, *Atg5*, *Ctsd*, and *CtsB* expression in quadriceps mRNA lysates from young (6 months old) male cTFEB;HSACre mice and controls.

(F) Immunoblot analysis for LAMP1 and Cathepsin D protein from young (5-6 months) and aged (22-24 months) control and cTFEB;HSACre quadriceps lysates mice of both sexes. Total Protein Stain Free lanes are shown as a loading control. Marker densitometry quantification relative to Protein Stain Free densitometry shown below.

(G) Representative images of gastrocnemius cross section from young (6-7 months old) control and cTFEB;HSACre female mice stained for LAMP1 (green), nuclei/Hoechst (blue). Quantification of LAMP1+ puncta and LAMP1+ area/muscle section for both sexes are shown on the right. Scale bars = 100 μm.

(H-I) Mitochondrial function measured by oxygen flux normalized to citrate synthase activity in soleus muscle from young (6 months old) and aged (18 months old) male (H) and female (I) control and cTFEB;HSACre semi-permeabilized soleus muscle. CI_P is complex I and CI+CII_P is complex I and II linked respiration coupled to ATP production. CI+CII_E is uncoupled complex I and II respiration or maximum respiration. CII_E is complex II respiration in the uncoupled state.

Each point represents the average of all data collected from an individual. Controls are age-matched littermates. All data were analyzed by 2-way between-subject (age × genotype) ANOVA with post hoc multiple comparisons, or one-way ANOVA and multiple comparisons post-hoc for each sex. Data are presented as mean ± SEM. * $p<0.05$, ** $p<0.01$. Lack of annotation indicates comparisons were not significant.

714 **Figure 3: Increased levels of known CNS-targeting myokines in TFEB-expressing skeletal**
715 **muscle**.
716 (A) VerSeDa-predicted secreted proteins identified as up-regulated or down-regulated in young
717 (green) and aged (blue) cTFEB;HSACre transgenic muscle, from proteomics studies from
718 Figure 2A-B.
719 (B) Immunoblot analysis for Cathepsin B protein in quadriceps protein lysates from young (5-6
720 months) and aged (22-24 months) control and cTFEB;HSACre quadriceps lysates mice of both
721 sexes. Note that the mature fragment of Cathepsin B is the secreted form. Total Protein Stain
722 Free lanes are shown as a loading control. Marker densitometry quantification relative to Protein
723 Stain Free densitometry shown below.
724 (C) Levels of cathepsin B in serum from young (5-6 months) and aged (22-24 months) control
725 and cTFEB;HSACre mice of both sexes.
726 Each point represents the average of technical replicates from an individual. Controls are age-
727 matched littermates. All data were analyzed by 2-way between-subject (age × genotype)
728 ANOVA with post hoc multiple comparisons, data are presented as mean ± SEM. * $p<0.05$, **
729 $p<0.01$. Lack of annotation indicates comparisons were not significant.
730
731 **Figure 4: Skeletal muscle TFEB-overexpression reduces accumulation of**
732 **hyperphosphorylated tau and microglial activation in a mouse model of tau pathology.**
733 (A) Immunoblot of 3x-FLAG TFEB protein in quadriceps muscle lysates from 9-month old MAPT
734 P301S;cTFEB;HSACre and MAPT P301S mice (top). Immunoblot for total Tau protein (T6
735 antibody) in hippocampal lysates from same individuals (bottom). GAPDH is shown below as a
736 loading control.
737 (B) Representative merged images of the hippocampus dentate gyrus stained for
738 phosphorylated tau (AT8, white) and nuclei/Hoechst (blue) in 9-month old control (top, in gold),
739 MAPT P301S (middle, in teal), and MAPT P301S;cTFEB;HSACre mice (bottom, in purple).
740 Insets depicting perinuclear AT8 staining are 5X zooms of areas demarcated by yellow squares.
741 Representative images are from male mice. Quantification of total phosphotau staining/section
742 (right, top) and for intracellular phosphotau staining, (right, bottom). Each point represents the
743 average of all sections containing the dentate gyrus (2-3 sections) for an individual animal.
744 Scale bars = 100 μm.
745 (C) Representative merged images of the dentate gyrus stained for astrocytes (GFAP, green),
746 microglia (IBA1, red) and nuclei (Hoechst, blue) in 9-month old control (top, gold), MAPT P301S
747 (middle, teal), and MAPT P301S;cTFEB;HSACre mice (bottom, purple). Insets depicting glia

748 morphology are 5X zooms of areas demarcated by yellow squares. Representative images are
749 from male mice. Quantification of IBA1+ microglia volume (top, right) and GFAP+ astrocyte
750 staining amounts per section (bottom, right). Each point represents the average of all sections
751 containing the dentate gyrus (2-3 sections) for an individual animal. Scale bars = 100 μm.
752 (D-E) Nanostring nCounter AD panel cluster analysis of differentially expressed genes for gene
753 clusters associated with microglial activation (D) and with trophic factors (E) in P301S MAPT
754 hippocampi (teal) compared to MAPT P301S;cTFEB;HSACre (purple) age-matched littermates
755 of both sexes. Analysis done via nSolver (Nanostring) differential gene expression analysis
756 software. Each point represents cluster scoring for a single individual hippocampal mRNA
757 lysate.
758 (F-G) qRT-PCR for *Bdnf* (F) and *Fndc5* (G) expression in hippocampal RNA lysates from 9-
759 month old male MAPT P301S (teal) and MAPT P301S;cTFEB;HSACre mice (purple) relative to
760 controls (not shown).
761 (H-I) Survival curves for male (H) and female (I) control (gold), MAPT P301S (teal), and MAPT
762 P301S;cTFEB;HSACre mice (purple).
763 Controls are littermates. Unless otherwise noted, data are represented as mean ± SEM. *
764 $p<0.05$, ** $p<0.01$,*** $p<0.001$, One-way ANOVA, post-hoc multiple comparisons (B,C), t-test
765 (D-G) and log-rank (Mantel-Cox) test (H-I). Lack of annotation indicates comparisons were not
766 significant.
767
768 **Figure 5: Skeletal muscle TFEB-overexpression decreases neuroinflammation, lipofuscin**
769 **accumulation, and improves cognitive performance in aged mice.**
770 (A-D) qRT-PCR for *Ccl2* (A), *Nfkb* (B), *Il6* (C), and *Bdnf* (D) expression in hippocampal mRNA
771 lysates from 18-month old cTFEB;HSACre mice and controls.
772 (E-F) Representative images dentate gyrus of the hippocampus stained for Hoechst (blue),
773 IBA1 (E, red, representative images are from females), and GFAP (F, green, representative
774 images are from males) in 18-22-month old control (top) and cTFEB;HSACre (bottom) mice.
775 Insets depicting glia morphology are 5X zooms of areas demarcated by yellow squares.
776 Quantification of IBA1+ microglial volume (E, top right) and IBA1+ branching index (E, bottom
777 right). Average number of GFAP+ astrocytes pixels per section (F, top) and GFAP+ astrocyte
778 branching index (F, bottom). Each point represents the average of all sections containing the
779 dentate gyrus from an individual. Scale bars = 100 μm.
780 (G) Representative merged images of the dentate gyrus of 18-22-month old control (top) and
781 cTFEB;HSACre (middle) mice stained for Hoechst (blue), and lipofuscin puncta

782 (autofluorescence, green, representative images are from females). Insets depicting
783 autofluorescent puncta within the dentate gyrus are 5X zooms of areas demarcated by yellow
784 squares. Scale bars = 100 μm.
785 (H-K) qRT-PCR for *Atg8* (H), *Lamp1* (I), *Sqstm1* (J), and *Ctsd* (K) expression in hippocampal
786 lysates from young (6 months old, closed diamonds) and aged (21 months old, open diamonds)
787 cTFEB;HSACre mice (purple diamonds) and controls (gold diamonds).
788 (L-Q) Neurocognitive phenotyping of aged (18 months old) cTFEB;HSACre and control animals.
789 Barnes maze (L,M), novel object recognition (N,O).
790 Controls are age-matched littermates. Each point represents the average of all data collected
791 from an individual. Data are represented as mean ± SEM. * $p<0.05$, ** $p<0.01$, One-way
792 ANOVA or two-way RMANOVA, post-hoc-tests. Lack of annotation indicates comparisons were
793 not significant.
794
795 **Figure 6: Transcriptome changes in the hippocampi of female cTFEB;HSACre transgenic**
796 **mice suggest synaptic remodeling and improved synaptic function.**
797 (A-B) Volcano plot of differentially expressed genes in hippocampal lysates from female young
798 (A, 6 months old) and aged (B, 24 months old) cTFEB;HSACre mice relative to controls.
799 (C-D) GO term analysis of differentially expressed genes from A and B including gene counts
800 and adjusted p values. Boxes highlight neurotrophic signaling pathways.
801 (E-F) KEGG analysis of differentially expressed genes from A and B. Number of differentially
802 expressed genes (DE) are shown above each category. Boxes highlight categories associated
803 with neural function.
804
805 **Figure 7: Transcriptome changes in the hippocampi of male cTFEB;HSACre transgenic**
806 **mice suggest activation of mitochondrial and ribosomal signaling.**
807 (A-B) Volcano plot of differentially expressed genes in hippocampal lysates from male young (A,
808 6 months old, 2 fold change) and aged (B, 24 months old, 1.25 fold change) cTFEB;HSACre
809 mice relative to controls.
810 (C-D) GO term analysis of differentially expressed genes from A and B including gene counts
811 and adjusted p values. Boxes highlight ribosomal and mitochondrial pathways.
812 (E-F) KEGG analysis of differentially expressed genes from A and B. Number of differentially
813 expressed genes (DE) are shown above each category. Boxes highlight ribosomal and
814 mitochondrial pathways.
815

816 **Supplemental Figures**

817

818 **Supplemental Figure 1: Skeletal muscle-restricted expression of human TFEB protein.**

819 (A-B) qRT-PCR analysis for human *TFEB* mRNA expression in 6-month old (A) and 21-24
820 month old (B) control and cTFEB;HSACre quadriceps skeletal muscle, heart ventricles and
821 hippocampus.

822 (C) Representative images of gastrocnemius cross sections stained for Hoechst (blue) and
823 Human TFEB (white). Insets of nuclear hTFEB staining are 5x zooms of the areas denoted by
824 the yellow squares. Scale bars = 100 μm.

825 (D-G) Immunoblot analysis for 3x-FLAG TFEB protein expression from lysates of brown adipose
826 (D), liver (E), heart ventricles (F), and brain (G) tissue from 6-month old female cTFEB;HSACre
827 mice and control littermates. cTFEB;HSACre skeletal muscle lysates are shown in the first lane
828 of each blot as a positive control for 3x-FLAG TFEB expression. FLAG-eGFP protein cassette
829 (arrow) as well as non-specific bands (asterisks) are indicated.

830 (H) Representative images of quadriceps and gastrocnemius cross sections from 7-week old
831 male TdTomato;HSACre transgenic mice stained for Hoechst (blue), TdTomato (red), and
832 Laminin (white). Scale bars = 100 μm.

833 (I) Representative images of hemibrain sections from 7-week old male TdTomato;HSACre
834 transgenic mice stained for Hoechst (blue), TdTomato (red). Insets of hippocampal regions are
835 5x zooms of the areas denoted by the yellow squares. Scale bars = 1 cm.

836 Controls are age-matched littermates. Each point represents the average of all data collected
837 from an individual. Data are represented as mean ± SEM. One-way ANOVA, post-hoc multiple
838 comparisons * $p<0.05$, ** $p<0.01$, *** $p<0.001$. Lack of annotation indicates comparisons were
839 not significant.

840

841 **Supplemental Figure 2: Fiber typing metrics in cTFEB;HSACre transgenic muscle.**

842 (A-H) Feret's minimum diameter (A-D) and fiber cross sectional area (E-H) of all 4 fiber types in
843 gastrocnemius muscle of young (7-9 months) and aged (22-24 months) control and
844 cTFEB;HSACre transgenic mice of both sexes.

845 (I) Immunoblot analysis for LC3 and total ubiquitin in quadriceps protein lysates from young (5-6
846 months) and aged (22-24 months) control and cTFEB;HSACre mice of both sexes. Total Protein
847 Stain Free lanes are shown as a loading control. Marker densitometry quantification relative to
848 Protein Stain Free densitometry shown below.

849 Controls are age-matched littermates. Each point represents the average of all data collected
850 from an individual. Data are presented as mean ± SEM. * $p<0.05$, ** $p<0.01$, **** $p<0.0001$
851 ANOVA and interactions of sex x age post-hoc. Lack of annotation indicates comparisons were
852 not significant.
853
854 **Supplemental Figure 3: Muscle-TFEB overexpression reduces hyperphosphorylated tau**
855 **accumulation and modifies expression of AD-associated genes in the hippocampus of**
856 **MAPT P301S transgenic mice.**
857 (A) Representative images of the hippocampal dentate gyrus from 9-month old control (top),
858 MAPT P301S (middle), and MAPT P301S;cTFEB;HSACre (bottom) mice stained for Hoechst
859 (blue) and AT180 PhosphoTau (white). Insets of hippocampal regions are 5x zooms of the
860 areas denoted by the yellow squares. Representative images are from males. Scale bars= 100
861 µm.
862 (B-C) Volcano plot of differentially expressed genes in the hippocampi of 9-month old male (B)
863 and female (C) MAPT P301S;cTFEB:HSACre animals relative to age-matched P301S MAPT
864 littermates using the Nanostring nCounter AD panel. Down-regulated genes in blue, up-
865 regulated genes in red.
866 (D) Cumulative ataxia score of 9-month old control, MAPT P301S, and MAPT
867 P301S;cTFEB;HSACre mice of both sexes.
868 (E) Weight (in grams) of 11-month old control MAPT P301S, and MAPT P301S;cTFEB;HSACre
869 mice of both sexes.
870 Controls are age-matched littermates. Each point represents the average of all data collected
871 from an individual. Data are represented as mean ± SEM. One-way ANOVA, post-hoc multiple
872 comparisons * $p<0.05$, ** $p<0.01$. Lack of annotation indicates comparisons were not significant.
873
874 **Supplemental Figure 4: Functional analysis of differentially expressed genes in the**
875 **hippocampus of female cTFEB;HSACre transgenic mice.**
876 (A-B) Reactome analysis of differentially expressed genes in hippocampal mRNA lysates from
877 female young (6 months old, A) and aged (24 months old, B) cTFEB;HSACre mice. Number of
878 differentially expressed genes (DE) are shown above each category.
879 (C-D) GO enrichment analysis of differentially expressed genes from A-B. Number of
880 differentially expressed genes (DE) are shown above each category.

881 (E) qRT-PCR analysis for select DE genes in hippocampal mRNA lysates from female young (6
882 months old, solid circles) and aged (24 months old, open circles) control (gold) and
883 cTFEB;HSACre (purple) mice. Expression levels normalized to young controls.
884 Controls are age-matched littermates. Each point represents the average of all data collected
885 from an individual. Data are represented as mean ± SEM, O One-way ANOVA, post-hoc
886 multiple comparisons, * $p<0.05$, ** $p<0.01$. Lack of annotation indicates comparisons were not
887 significant.
888
889 **Supplemental Figure 5: Functional analysis of differentially expressed genes in the**
890 **hippocampus of male cTFEB;HSACre transgenic mice**
891 (A-B) Reactome analysis of differentially expressed genes in hippocampal mRNA lysates from
892 male young (6 months old, A) and aged (24 months old, B) cTFEB;HSACre mice. Number of
893 differentially expressed genes (DE) are shown above each category.
894 (C-D) GO enrichment analysis of differentially expressed genes from A-B. Number of
895 differentially expressed genes (DE) are shown above each category.
896 (E) qRT-PCR analysis for select DE genes in hippocampal mRNA lysates from female young (6
897 months old, solid circles) and aged (24 months old, open circles) control (gold) and
898 cTFEB;HSACre (purple) mice. Expression levels normalized to young controls.
899 Controls are age-matched littermates. Each point represents the average of all data collected
900 from an individual. Data are represented as mean ± SEM, One-way ANOVA, post-hoc multiple
901 comparisons, * $p<0.05$, ** $p<0.01$. Lack of annotation indicates comparisons were not
902 significant.
903
904 **Supplemental Figure 6: Overlap of differentially expressed genes confirms sex-specific**
905 **transcriptional remodeling in the hippocampus of TFEB;HSACre transgenic mice.**
906 (A) Overlap of differentially expressed genes (DEGs) in hippocampal mRNA lysates from young
907 (6 months old) cTFEB;HSACre mice relative to their age-matched controls. Number of up- or
908 down-regulated DEGs are shown next to each unique and shared category.
909 (B) Overlap of differentially expressed genes (DEGs) in hippocampal mRNA lysates from aged
910 (24 months old) cTFEB;HSACre mice relative to their age-matched controls. Number of up- or
911 down-regulated DEGs are shown next to each unique and shared category.

912 **STAR★Methods**

913 **Key resources table**

REAGENT or RESOURCE	SOURCE	IDENTIFIER
Antibodies		
Mouse monoclonal anti-FLAG® M2	Sigma-Aldrich	RRID: AB_262044
Rabbit anti-TFEB	Cell Signaling Technology	RRID: AB_11220225
Rabbit monoclonal anti-LC3A/B	Cell Signaling Technology	RRID: AB_2617131
Mouse IgG1 monoclonal anti-GAPDH	Invitrogen	Cat #: AM4300
Rat IgG2a monoclonal anti-LAMP1	DSHB	Cat #: 1D4B
Rabbit anti-SQSTM1/p62	Cell Signaling Technology	Cat #: 5114T
Mouse monoclonal anti-Ubiquitin	Santa Cruz Biotechnology	RRID: AB_628423
Rabbit polyclonal anti-Cathepsin B (H190)	Cell Signaling Technology	RRID: AB_2292384
Goat polyclonal anti-Cathepsin D (C-20)	Santa Cruz	RRID: AB_637896
Chicken polyclonal anti-GFAP	Abcam	RRID: AB_304558
Rabbit polyclonal anti-IBA1	FUJIFILM Wako Shibayagi	RRID: AB_839504
Mouse monoclonal anti-Phospho-Tau (Thr231) (AT180)	Thermo Fisher Scientific	RRID: AB_223649
Mouse monoclonal anti-Phospho-Tau (Ser202, Thr205) (AT8)	Thermo Fisher Scientific	RRID: AB_223647
Rabbit polyclonal anti-Laminin	Abcam	RRID: AB_298179
Rabbit polyclonal anti-LC3B	Cell Signaling Technology	RRID: AB_915950
Guinea Pig polyclonal anti-p62	Progen	RRID: AB_2687531
Mouse monoclonal anti-Myosin Heavy Chain Type I	DSHB	RRID: AB_2235587
Mouse monoclonal anti-Myosin Heavy Chain Type IIA	DSHB	RRID: AB_2147165
Mouse monoclonal anti-Myosin Heavy Chain Type IIB	DSHB	RRID: AB_2266724
Bacterial and virus strains		
pCMV-human TFEB (NM_007162) Human Untagged Clone	Origene	CAT#: SC122773
Chemicals, peptides, and recombinant proteins		
2,2,2-Tribromoethanol ≥99%	VWR	Cat #: BT145585
2-Methyl-2-butanol 99%	VWR	Cat #: TS16662-0010
TRIzol	Invitrogen	Cat #: 15596026
Turbo DNase	Thermo Fisher	Cat #: AM2238
Sybrgreen	Life Technologies	Cat #: 4309155

RIPA Lysis and Extraction Buffer	Invitrogen	Cat #: 89900
1X Halt™ Protease and Phosphatase Inhibitor Cocktail	Invitrogen	Cat #: 78442
iScript™ cDNA Synthesis Kit	BioRad	Cat #: 1708891
SYBR™ Green PCR Master Mix	Life Technologies	Cat #: 4309155
Critical Commercial Assays		
Pierce™ BCA Protein Assay Kits	Invitrogen	Cat #: 23225
Mouse Cathepsin B ELISA Kit	Abcam	Cat #: ab303743
Deposited data		
TFEB Muscle proteomics	Panorama Public	ID: PXD045241
Hippocampal Bulk RNA-seq data	GEO	GEO: GSE242363
Experimental models: Organisms/strains		
Mouse: fxSTOP-TFEB	This paper	N/A
Mouse: HSA-Cre (FVB.Cg-Tg(ACTA1-cre)79Jme/J)	JAX Judith Melki	RRID: IMSR_JAX:006139
Mouse: TdTomato (B6.Cg-Gt(ROSA)26Sortm9(CAG-tdTomato)Hze/J	JAX Philippe Soriano	RRID: IMSR_JAX:007909
Mouse: MAPT P301S (B6;C3-Tg(Prnp-MAPT*P301S)PS19Vle/J)	JAX Virginia Lee	RRID: IMSR_JAX:008169
Oligonucleotides		
Actb	IDT	Mm.PT.39a.22214843.g
Lamp1	Biorad	10025636
Atg5	IDT	Mm.PT.58.29236732
CTSD	IDT	Mm.PT.58.7639164
CTSB	IDT	237299388
Fndc5	IDT	Mm.PT.58.31333197
BDNF	IDT	Mm.PT.58.28814650
Ccl2	IDT	287573375
NFkB1	IDT	287573349
IL6	IDT	Mm.pt.58.10005566
Atg8 -LC3/ Map1lc3b		Mm.PT.58.29764292
Sqstm1	IDT	Mm.PT.58.5854953
Human TFEB	IDT	Hs.PT.58.50432039
Oprd1	IDT	Mm.PT.58.41742748
CCL3/MIP-1alpha	IDT	Mm.PT.58.29283216
Hgf	IDT	Mm.PT.58.43661644.g

Gpr88	IDT	Mm.PT.58.43661644.g
Stap1	IDT	Mm.PT.58.31635149
Gabrr2	IDT	Mm.PT.58.6928777
Pomc	IDT	Mm.PT.58.5917321
Fosb	IDT	Mm.PT.58.10990878
S100a8	IDT	Mm.PT.58.44003402.gs
S100a9	IDT	Mm.PT.58.41787562
Gnb3	IDT	Mm.PT.58.33035404
Tlr8	IDT	Mm.PT.58.16021150
Romo1	IDT	Mm.PT.56a.11138846
Software and algorithms		
FIJI	Schindelin et al.[76]	https://imagej.net/software/fiji/
QuantStudio 3	Applied Biosystems	RRID:SCR_018712
STRING Version 12.0	STRING Consortium	RRID: SCR_005223
NanoString nCounter Analysis System	NanoString	RRID:SCR_021712

Resource availability

Lead contact

Further information and requests for resources and reagents should be directed to and will be fulfilled by the lead contact, Constanza Cortes (cjc_149@usc.edu).

Materials availability

The fxSTOp-TFEB line of transgenic mice is available for sharing with academic institutions free-of-charge. For-profit institutions will adhere to UCSD's policy regarding copyrighted material.

Data and code availability

- Bulk RNA-seq data have been deposited at GEO and are publicly available as of the date of publication. Accession numbers are listed in the key resources table. Muscle proteomics data have been deposited at Panorama Public and are publicly available as of the date of publication. ID numbers are listed in the key resources table. Microscopy data reported in this paper will be shared by the lead contact upon request.
- This paper does not report original code.
- Any additional information required to reanalyze the data reported in this work paper is available from the lead contact upon request.

Experimental model details

Mouse models used were the novel fxSTOP-TFEB transgenic line generated for this publication, the HSA-Cre transgenic mice (JAX Strain No: 006139 | HSA-Cre79) obtained from JAX, TdTomato mice (B6.Cg-Gt(ROSA)26Sor$^{tm9(CAG\text{-}tdTomato)Hze/J}$, JAX Strain #:007909) also from JAX, and the MAPT P301S line (Stock No: 008169) which originated in the laboratory of Dr. Virginia Lee. All animals have the C57BL/6J genetic background, both males and females were used wherever possible.

Method details

Generation of fxSTOP-TFEB transgenic mice.

We used a pCMV-human TFEB expressing vector from Origene (clone # sc122773), used previously [27]. We cloned a 3x-FLAG fragment via insertion into the Acc65I and Pac1 restriction sites of the targeting vector. The fxSTOP-TFEB vector was generated in multiple steps, as follows: (1) 5′ and 3′ targeting arms were inserted by PCR onto the ends of a minimal 1.8 kb, chloramphenicol-resistant vector; (2) an ampicillin resistance cassette was cloned into the MluI, XmaI sites of the targeting vector; (3) an 1.1 kb fragment encoding the actin promoter, a loxP site, a 3x-FLAG tag fused to EGFP was cloned into the NheI, PacI restriction sites of the targeting vector; (4) a 2.8 kb fragment containing the second loxP site, followed by 3x-FLAG-human TFEB sequence. The final fxSTOP-FLAG-human TFEB vector was microinjected into C57BL/6J:C3H/HeJ F1 hybrid oocytes. Of six founders identified, two gave rise to fxSTOP-FLAG-human TFEB lines with comparable phenotypes. Of these lines, we chose to focus our

956 studies principally on line 419. The presence of the floxed 3x-FLAG-eGFP STOP-3x-FLAG-
957 human TFEB cassette is verified by allele dependent qPCR genotyping analysis with each
958 generation (Transnetyx), and expression of the 3x-FLAG-eGFP sequence (upstream of the
959 STOP codon) in single transgenic fxSTOP-TFEB mice is assessed every other generation. We
960 confirmed excision of 3x-FLAG-EGFP-STOP cassette in the presence of Cre-recombinase by
961 crossing fxSTOP-TFEB transgenic female mice with HSA-Cre transgenic mice (JAX Strain No:
962 006139 | HSA-Cre79), and corresponds to the HSA-Cre driver mouse line from the laboratory of
963 Dr. Judith Melki. TdTomato mice (B6.Cg-Gt(ROSA)26Sor$^{tm9(CAG\text{-}tdTomato)Hze/J}$, JAX Strain
964 #:007909) express robust tdTomato fluorescence following Cre-mediated recombination, is
965 congenic on the C57BL/6J genetic background and were also obtained from JAX. The MAPT
966 P301S line (Stock No: 008169) originated in the laboratory of Dr. Virginia Lee.
967 cTFEB;HSACre;MAPT P301S transgenic mice were generated by crossing fxSTOP-TFEB
968 females to MAPT P301S males. Double transgenic offspring was then crossed with
969 heterozygote HSA-Cre transgenic individuals. All commercially available lines were obtained
970 directly from JAX. All lines have been maintained in a C57/B6 background for over ten
971 generations in our lab. Mice were housed in a temperature- and humidity-controlled
972 environment on a 12-hour light/dark cycle with food and water ad libitum. Mice of both sexes
973 were used for all experiments in equal numbers, or as close to equal numbers as possible. For
974 all MAPT P301 experiments, control animals are MAPT P301S;fxSTOP-TFEB-;HSACre- and/or
975 MAPT P301S;fxSTOP-TFEB+;HSACre- littermates. For all aging experiments, control animals
976 are fxSTOP-TFEB-;HSACre- and/or fxSTOP-TFEB+;HSACre- littermates. In our hands, we did
977 not detect any differences on tau or aging-associated CNS phenotypes on fxSTOP-TFEB+
978 animals compared to the wild-type controls. All animal experimentation adhered to NIH
979 guidelines and was approved by and performed in accordance with the University of California,
980 San Diego, Duke University, University of Alabama at Birmingham, and the University of
981 Southern California Institutional Animal Care and Use.

982 **Tissue Collections.**

983 Animals were anesthetized with 3.8% Avertin Solution. All animals received a transcardial
984 perfusion with 60 mLs of cold 1x PBS. Half of CNS tissue (right/left hemi-brain) was post-fixed in
985 4% PFA for less than 24 hours before being transferred to 30% sucrose for another 24 hours
986 before cryo-sectioning and staining the other half was micro-dissected into cortex and
987 hippocampus and flash-frozen in liquid nitrogen for RNA and protein analyses. Half of skeletal

988 muscle tissue (right/left limb muscle) was fresh frozen in OCT following dissection, while the
989 other half was flash-frozen in liquid nitrogen for RNA and protein analyses.

990 **RT-PCR Analysis.**

991 Flash frozen perfused isolated mouse tissues (quadriceps, hippocampus) were placed in plastic
992 tubes with silica beads (MP Biomedical, 116913100) and homogenized in the FastPrep-24™ 5G
993 bead beating grinder and lysis system (MP Biomedical, 116005500) in TRIzol (Invitrogen,
994 15596026). RNA was extracted via standard phenol-chloroform procedures followed by DNase
995 digestion (ThermoFisher, AM2238). cDNA was generated using iScript (Bio-Rad Technologies,
996 1708891). Quantitative PCR was run using Sybrgreen (Life Technologies, 4309155) for
997 chemical detection (Applied Biosystems; QuantStudio 3). Enrichment was determined based on
998 double-delta CT value. Primers were ordered from IDT Predesigned qPCR Assays unless
999 otherwise specified. Primers used are listed in the Key Resources Table.

1000 **Protein Extraction and ImmunoBlot Analysis.**

1001 Protein lysates from muscle tissue was prepared as previously described [27,28]. In short, Flash
1002 frozen perfused isolated mouse tissues (quadriceps, hippocampus) were placed in plastic tubes
1003 with silica beads (MP Biomedical, 116913100) and homogenized in the FastPrep-24™ 5G bead
1004 grinder and lysis system (MP Biomedical, 116005500) in RIPA Lysis and Extraction Buffer
1005 (Invitrogen, 89900), 1X Halt™ Protease and Phosphatase Inhibitor Cocktail (Invitrogen, 78442),
1006 and 1% SDS. Protein concentration was quantified using a Pierce™ BCA Protein Assay
1007 (23227). For brain tissue, Fifty or 25 µg of homogenized proteins were loaded per lane, and
1008 after running Any KD, 10%, or 4-15% Mini-PROTEAN TGX Gels (BioRad, 4568124, 4561034,
1009 and 4561084), samples were transferred to 0.45 µm PVDF membranes (BioRad, 1704275),
1010 which were blocked in 5% BSA in PBS at RT for 1 hr. For skeletal muscle, proteins were
1011 separated on 4-20% Stain-Free TGX gels (Bio-Rad, 5678092), separated to PVDF, and blocked
1012 in 5% non-fat dry milk in TBST (1X TBS with 0.05% Tween-20) for 1 hour at RT. Membranes
1013 were incubated with anti-FLAG antibody (Sigma, M2, F1804, 1:1000), anti-TFEB antibody (Cell
1014 Signaling, 4240,1:1000), anti-Lamp1 antibody (DSHB, 1DB4, 1:1000), anti-LC3A/B antibody
1015 (Cell Signaling, 12741, 1:1000), anti-P62 antibody (Cell signaling, 5114T, 1:1000), anti-ubiquitin
1016 antibody (Santa Cruz, sc-8017, 1:1000), anti-Cathepsin B antibody (Cell signaling, 3383S,
1017 1:1000), anti-Cathepsin D antibody (Santa Cruz, sc-6486, 1:1000),or anti-GAPDH (Invitrogen,
1018 AM4300, 1:5000) in PBS-T with 5% BSA at 4°C overnight. The primary antibody was visualized

1019 with horseradish-peroxidase conjugated anti-rabbit at (Cell Signaling, 7074P2, 1:5,000) and
1020 enhanced chemiluminescence (BioRad, 170-5060) or goat-anti-mouse IgG 680 (Invitrogen,
1021 A21058, 1:10,000). Densitometry analysis was performed using the BioRad Image Lab 6.1
1022 software application.

1023 **Immunofluorescence Studies.**

1024 Tissue was embedded in OCT (TissueTek, 4583), frozen utilizing 2-methylbutane (VWR,
1025 103525-278) submerged in liquid nitrogen and stored at -80 C until used. All samples were
1026 sectioned on a standing cryostat (Leica). Brain sections were 20 microns thick, while muscle
1027 sections were 15 microns thick. For immunohistochemistry, sections were permeabilized with
1028 .25% Triton for 15 mins and blocked with 4% BSA for 30 minutes-1 hour. Brain sections were
1029 then incubated with anti-GFAP (ab4674, Abcam, 1:200), anti-IBA1 (Wako, 019-19741, 1:200),
1030 anti-AT180 TAU (ThermoFisher, MN1040, 1:100) and anti-AT8 TAU (ThermoFisher, MN1020,
1031 1:100) while muscle sections were incubated with anti-laminin (Abcam, ab11575, 1:200), anti-
1032 FLAG (Sigma, F1804, 1:1000), anti-LC3B (Cell Signaling, 2775S, 1:200), anti-LAMP1 (Novus,
1033 NB100-77685, 1:200), anti-p62 (Progen, GP62-C, 1:200), anti-MHC Type 1 (DSHB, BD-D5,
1034 1:100), anti-MHC Type 2A (DSHB, SC-71, 1:100), anti-MHC Type 2B (DSHB, BF-F3, 1:100),
1035 and anti-hTFFEB (CST, 4240, 1:200) overnight at 4°C and incubated with secondary antibodies
1036 at RT for 1 hour (both diluted in 4% BSA). Next the slides were washed with Hoescht
1037 (ThermoFisher, 62249, 1:5000) and mounted with prolong glass (Invitrogen, P36984). All slides
1038 were washed with 1X PBS three times for 5 minutes each between steps.

1039 Slides with brain sections stained for TAU and glia markers were imaged in the UAB HIRF HRIF
1040 Confocal/Light Microscopy Core utilizing the 10x objective on the Nikon A15R/SIM Confocal
1041 microscope. Z-stacks of the entire hippocampus area/section were collected, and max intensity
1042 projections were generated using FIJI. Lipofuscin imaging was performed using an
1043 epifluorescent Nikon light microscope with a 20x objective. For TdTomato imaging, stitched
1044 whole-section z-stacks were acquired using a Nikon A1R HD25 confocal microscope of nuclei in
1045 the blue channel and native TdTomato fluorescence in the red channel. Muscle sections were
1046 imaged with an ECHO Revolution epifluorescent microscope.

1047 For quantification of astrocyte and/or microglia parameters, NIS elements was used to collect
1048 morphometric information and numbers. A size exclusion parameter was used for GFAP
1049 positive objects under 10 microns, IBA-1 positive objects under 15 microns, and any object

1050 larger than 5,000 microns were all excluded due to standard assessments of cell sizes. FIJI was
1051 used for quantification of lipofuscin and LAMP1 puncta. Muscle fibertype composition, number,
1052 and size were quantified using Myosoft [77], a FIJI plugin.

1053 **Quantitative Proteomics Sample Preparation and Data-independent Acquisition Mass**
1054 **Spectrometry.**

1055 *Lysis/Digestion*

1056 We identified distinct protein species from crude total extractions of whole quadricep muscle by
1057 mass spectrometry. Quadricep muscle powder lysate in 50 mM ammonium bicarbonate with
1058 0.1% RapiGest (Waters, Cat# 186001861) were processed and digested using Qiagen Tissue
1059 Lyser II (Qiagen) following the manufacturer's protocol. Protein concentrations were determined
1060 using Pierce BCA Protein Assay Kit (ThermoFisher, PI23227). 150 µg of lysate was reduced
1061 with DTT (Sigma, Cat # D0632), alkylated with IAA (Sigma, Cat # D0632) and digested at 1 µg
1062 trypsin (Thermo, Cat # PI-90057) to 50 µg protein ratio for 16 hours at 37°C. Digests were
1063 acidified with 200 mM HCl (Fisher, Cat # A144), cleaned with MCX columns (Waters, Cat#
1064 186000782), dried with a vacuum concentrator, and reconstituted in 0.1% formic acid (Fisher,
1065 Cat# A117) in water.

1066 *Liquid Chromatography and Mass Spectrometry*

1067 One µg of each sample with 150 fmol of Pierce Retention Time Calibrant (PRTC, Thermo, Cat #
1068 PI-88321) was loaded onto a 30 cm fused silica picofrit 75 µm column (New Objective, Woburn,
1069 MA, Cat # PF3607510N5) and 3.5 cm 150 µm fused silica Kasil1 (PQ Corporation) frit trap
1070 loaded with 3 µm Reprosil-Pur C18 (ESI Source Solutions, Cat # r13.aq.0001) reverse-phase
1071 resin analyzed with a Thermo Easy nano-LC 1000 coupled to a Thermo Orbitrap Fusion Lumos
1072 Mass Spectrometer. Data-independent (DIA) mass spectrometry with gas-phase fractionation
1073 was performed as described previously [78,79].

1074 *Data Analysis*

1075 Thermo DIA MS/MS RAW files were converted to mzML format using Proteowizard (version
1076 3.0.19045) [80] using vendor peak picking and demultiplexing. Chromatogram spectral libraries
1077 were created using default settings (10 ppm tolerances, trypsin digestion, HCD b- and y-ions) of
1078 Walnut in EncyclopeDIA (version 0.6.14) [81] using the Uniprot mouse canonical FASTA [82].

1079 Quantitative spectral libraries were created by mapping spectral to the chromatogram spectral
1080 library using EncyclopeDIA requiring a minimum of 3 quantitative ions and filtering peptides at a
1081 1% FDR using Percolator 3.01 [83]. The quantitative spectral library is imported into Skyline-daily
1082 4.2.1.19058 [84] with the Uniprot mouse canonical FASTA as the background proteome to map
1083 peptides to proteins. The mzML data is imported and all data is TIC normalized.

1084 *Data and code availability*

1085 The Skyline document and raw files for the proteomics DIA MS/MS data are available at
1086 Panorama Public [85]. ProteomeXchange ID: PXD045241. Access URL:
1087 https://panoramaweb.org/mouse-muscle-TFEB-proteomics.url. All original data has been
1088 deposited at Panorama and is publicly available as of the date of publication. Any additional
1089 information required to reanalyze the data reported in this paper is available from the lead
1090 contact upon request.

1091 **High-Resolution Respirometry and ROS Production.**

1092 High-resolution respirometry (HRR) was conducted on a G-model Oxygraph-2k machine
1093 (Oroboros Instruments, Innsbruck, Austria). Reagents, muscle fiber preparation, and Substrate
1094 Uncoupler Inhibitor Titration (SUIT) protocols used for HRR have been previously described [86].
1095 Antimycin A was sufficient to block complex 3 activity; therefore, myxothiazol was not added in
1096 our SUIT protocol. ROS production was detected using the O2k-Fluo (Oroboros Instruments)
1097 and a modified Amplex Red assay. After daily background correction, chambers were closed
1098 and 20 μM final concentration Amplex Red ultra (Life Technologies, A36006), 1 U/mL
1099 horseradish peroxidase (Sigma-P8250), and 5 U/mL superoxide dismutase (Sigma-S8409)
1100 were added to the wells. After the amp-slope stabilized 0.1 μM H2O2 (Sigma-95321) was added
1101 for calibration. Throughout the entire assay, repeated injections of 0.1 μM H2O2 were used for
1102 calibration including one injection after the muscle tissue was added to correct for
1103 autofluorescence. All subsequent 0.1 μM H2O2 injections were used to control for changing
1104 concentrations of Amplex Red during the assay. Samples for HRR aere conducted in duplicate
1105 and means were used for the final analyses. To eliminate confounds from tissue damage or
1106 hyperpermeabilization, only samples with stable oxygen flux and Raw-amps were included in
1107 the final analysis.

1108 **Gene Expression Analysis.**

1109 *RNA Sequencing and Bioinformatics Analysis*

1110 RNA was extracted as mentioned above from flash frozen hippocampal tissue for four biological
1111 replicates (sex/genotype) and checked for quality by bioAnalyzer by Novogene (Novogene
1112 Corporation INC, Sacramento, CA, United States). mRNA libraries were prepared by Novogene
1113 using poly-T oligo-attached magnetic beads. cDNA was synthesized with random hexamer
1114 primers and dUTP or dTTP depending on library directionality. For the both non-directional and
1115 directional library prep; end repair, A-tailing, adapter ligation, size selection, amplification, and
1116 purification were performed. For the directional library, end repair, USER enzyme digestion was
1117 also performed. Libraries were checked via Qubit and qPCR for quantity and by bioanalyzer for
1118 size. Quantified libraries were pooled and bulk RNA-seq analysis was performed via NovaSeq
1119 PE150 (Illumina, San Diego, CA, United States) high throughput sequencing. Bioinformatics
1120 analysis for differentially expressed genes was performed by Novogene. Raw reads were
1121 cleaned to remove adapters, poly-N and low qualities reads from the data. The reference index
1122 was built using Hisat2 v2.05 and pair-end cleaned reads were aligned to the reference genome
1123 GRCm39 through Hisat2 v2.05. reads were counted using featureCounts v1.5.0-p3. FPKM of
1124 each gene was calculated based on the length of the gene and read counts mapped. Differential
1125 expression analysis was performed using the DEseq2 R package (1.20.0). Gene Ontology (GO)
1126 and KEGG enrichment analysis of differentially expressed genes was implemented by the
1127 clusterProfiler R package. For all analysis methods and graphic representations, a p-value less
1128 than 0.05 was considered significantly enriched by differentially expressed genes. For young (6-
1129 month) animals, a 2-fold change was used to determine differentially expressed genes. A 1.2
1130 fold change was used for aged (24-month) animals. Volcano plots were generated in RStudio
1131 using ggplot2 using these criteria.

1132 *Nanostring nCounter AD panel*

1133 Assays were performed with 100 ng aliquots of RNA, extracted using the PureLink RNA
1134 extraction kit (Invitrogen) and run via the NanoString nCounter Analysis system (NanoString
1135 Technologies, Seattle, WA, USA) at the UAB Nanostring Core, following previously described
1136 and established protocols[54]. After codeset hybridization overnight, the samples were washed
1137 and immobilized to a cartridge using the NanoString nCounter Prep Station. Cartridges were
1138 scanned in the nCounter Digital Analyzer at 555 fields of view for the maximum level of
1139 sensitivity. Raw reads and the Nanostring Mm_AD30_v1.1 probe annotation codeset were
1140 imported into the Nanostring proprietary software, nSolver 4.0, and QC was performed following

company protocol guidelines. Counts for target genes were normalized to house-keeping genes included in the panel (Cltc, Gapdh, Gusb, Hprt, Pgk1, and Tubb5). Specifically, background correction was performed using the negative control at the cutoff of mean + 2 standard deviation. Housekeeping genes were used for normalization based on geometric mean, Gene expression was normalized using NanoStringNorm R package. All p-values were adjusted using a false discovery rate (FDR) correction of 1% for multiple comparisons. Differential expression and pathway scoring analysis, as well as graphical QC representation were performed in the nSolver Advanced Analysis Software 2.0 using a custom analysis to utilize generated normalized counts. Differential gene expression values were presented asMAPT P301S baseline compared to the MAPT P301S;cTFEB;HSACre cohort for each sex, and a p value of 0.05 or less was described as significant. Volcano plots were generated with ggplot2 in Rstudio using significant genes and a cutoff of 1.2 or greater fold change. The pathway scoring module summarizes a single score from the data from a pathway's genes [87].

Data and code availability

Bulk RNA-seq data have been deposited at GEO and are publicly available as of the date of publication. Accession numbers (GSE242363) are listed in the key resources table. No new code was generated or used in the analysis of this dataset. Any additional information required to reanalyze the data reported in this paper is available from the lead contact upon request.

Cathepsin B ELISA Analysis.

Fifty µl of serum (collected via blood cardiac puncture and isolated via standard coagulation/centrifugation protocols) was diluted 1:1 and processed with the Cathepsin B ELISA kit (Abcam, ab119585). Diluted samples were processed following kit instructions, and imaged at 450 nm (Tecan, Infinite M plex). Amount of cathepsin B was determined using a standard dilution curve of known concentration.

Mouse Phenotyping and Behavioral Studies.

Barnes Maze

The Barnes maze apparatus is an opaque Plexiglas disc 75 cm in diameter elevated 58 cm above the floor by a tripod. Twenty holes, 5 cm in diameter, are located 5 cm from the perimeter, and a black Plexiglas escape box (19 x 8 x 7 cm) is placed under one of the holes.

Distinct spatial cues are located all around the maze and are kept constant throughout the study. On the first day of testing, a training session was performed, which consists of placing the mouse in the escape box for one minute. After the one-minute habituation period, the first session was started. At the beginning of each session, the mouse was placed in the middle of the maze in a 10 cm high cylindrical black start chamber. After 10 seconds the start chamber was removed, a buzzer (80 dB) and a light (400 lux) were turned on, and the mouse was set free to explore the maze. The session ended when the mouse entered the escape tunnel or after 3 min elapsed. When the mouse entered the escape tunnel, the buzzer was turned off and the mouse was allowed to remain in the dark for one minute. When the mouse did not enter the tunnel by itself it was gently put in the escape box for one minute. The tunnel was always located underneath the same hole (stable within the spatial environment), which was randomly determined for each mouse. Mice were tested once a day for 4 days for the acquisition portion of the study. For the 5th test (probe test), the escape tunnel was removed and the mouse was allowed to freely explore the maze for 3 min. The time spent in each quadrant was determined and the percent time spent in the target quadrant (the one originally containing the escape box) was compared with the average percent time in the other three quadrants. This was a direct test of spatial memory as there was no potential for local cues to be used in the mouse's behavioral decision. Two weeks later the mice were tested again with the escape box in the original position (retention test). This allows for the examination of long-term memory. Finally, on the day after this test, the escape tunnel was moved to a new location (90 degrees from the original position) and the behavior of the mouse was recorded. This is called the reversal test and it allows for the examination of perseveration at the old hole as well as the working memory strategies the mice adopted to locate the new tunnel location. Each session was videotaped and scored by an experimenter blind to the genotype of the mouse. Measures recorded include the latency to enter the escape box and the number of errors made per session. Errors are defined as nose pokes and head deflections over any hole that did not have the tunnel beneath it. The probe data were analyzed using Noldus Ethovision software to determine time spent in each quadrant of the maze as well as to assess activity measures.

Novel Object Recognition

Mice were individually habituated to a 51cm x 51cm x 39cm open field for 5 min. Mice were then tested with two identical objects placed in the field (either two 250 ml amber bottles or two clear plastic cylinders 6x6x16cm half filled with glass marbles). An individual animal was allowed to explore for 5 min, now with the objects present. After two such trials (each separated by 1

minute in a holding cage), the mouse was tested in the object novelty recognition test in which a novel object replaced one of the familiar objects (for example, an amber bottle if the cylinders were initially used). All objects and the arena were thoroughly cleaned with 70% ethanol between trials to remove odors. Behavior was video recorded and then scored for number contacts (touching with nose or nose pointing at object and within 0.5 cm of object) and/or for time contacting the objects. Habituation to the objects across the familiarization trials (decreased contacts) was an initial measure of learning and then renewed interest (increased contacts) in the new object indicated successful object memory. Recognition indexes were calculated using the following formula: (# contacts during test)/(# contacts in last familiarization trial + # contacts during test). Values greater than 0.5 indicate increased interest, whereas values less than 0.5 indicate decreased interest in the object during the test relative to the final familiarization trial. quadrant of the maze as well as to assess activity measures.

Quantification and statistical analysis

All data were analyzed by t-test, 1-way, 2-way or 3-way between-subject ANOVA with post hoc comparisons depending on the number of variables and groups in each analysis. For ANOVA, if statistical significance ($p < 0.05$) was achieved, we performed post hoc analysis to account for multiple comparisons. The level of significance (α) was always set at 0.05. Survival curves were analyzed using Log-rank (Mantel-Cox) Test. Data were analyzed using Prism 7 (GraphPad Software, La Jolla, CA) and are represented as means and standard error of the means. All experiments and data analyses were conducted in a blinded fashion. All data were prepared for analysis with standard spread sheet software (Microsoft Excel).

REFERENCES

1 Lopez-Otin, C., Blasco, M. A., Partridge, L., Serrano, M. & Kroemer, G. Hallmarks of aging: An expanding universe. *Cell* **186**, 243-278, doi:10.1016/j.cell.2022.11.001 (2023).

2 Mattson, M. P. & Arumugam, T. V. Hallmarks of Brain Aging: Adaptive and Pathological Modification by Metabolic States. *Cell Metab* **27**, 1176-1199, doi:10.1016/j.cmet.2018.05.011 (2018).

3 Ham, S. & Lee, S. V. Advances in transcriptome analysis of human brain aging. *Exp Mol Med* **52**, 1787-1797, doi:10.1038/s12276-020-00522-6 (2020).

4 Demontis, F., Patel, V. K., Swindell, W. R. & Perrimon, N. Intertissue control of the nucleolus via a myokine-dependent longevity pathway. *Cell Rep* **7**, 1481-1494, doi:10.1016/j.celrep.2014.05.001 (2014).

5 Rai, M. *et al.* Proteasome stress in skeletal muscle mounts a long-range protective response that delays retinal and brain aging. *Cell Metab* **33**, 1137-1154.e1139, doi:10.1016/j.cmet.2021.03.005 (2021).

6 Durieux, J., Wolff, S. & Dillin, A. The cell-non-autonomous nature of electron transport chain-mediated longevity. *Cell* **144**, 79-91, doi:10.1016/j.cell.2010.12.016 (2011).

7 Taylor, R. C. & Dillin, A. XBP-1 is a cell-nonautonomous regulator of stress resistance and longevity. *Cell* **153**, 1435-1447, doi:10.1016/j.cell.2013.05.042 (2013).

8 Demontis, F. & Perrimon, N. FOXO/4E-BP signaling in Drosophila muscles regulates organism-wide proteostasis during aging. *Cell* **143**, 813-825, doi:10.1016/j.cell.2010.10.007 (2010).

9 van Oosten-Hawle, P., Porter, R. S. & Morimoto, R. I. Regulation of organismal proteostasis by transcellular chaperone signaling. *Cell* **153**, 1366-1378, doi:10.1016/j.cell.2013.05.015 (2013).

10 Villeda, S. A. *et al.* The ageing systemic milieu negatively regulates neurogenesis and cognitive function. *Nature* **477**, 90-94, doi:10.1038/nature10357 (2011).

11 Conboy, I. M. *et al.* Rejuvenation of aged progenitor cells by exposure to a young systemic environment. *Nature* **433**, 760-764, doi:10.1038/nature03260 (2005).

12 Castellano, J. M. *et al.* Human umbilical cord plasma proteins revitalize hippocampal function in aged mice. *Nature* **544**, 488-492, doi:10.1038/nature22067 (2017).

13 Schaum, N. *et al.* Ageing hallmarks exhibit organ-specific temporal signatures. *Nature* **583**, 596-602, doi:10.1038/s41586-020-2499-y (2020).

14 Villeda, S. A. *et al.* Young blood reverses age-related impairments in cognitive function and synaptic plasticity in mice. *Nat Med* **20**, 659-663, doi:10.1038/nm.3569 (2014).

15 De Miguel, Z. *et al.* Exercise plasma boosts memory and dampens brain inflammation via clusterin. *Nature*, doi:10.1038/s41586-021-04183-x (2021).

16 Horowitz, A. M. *et al.* Blood factors transfer beneficial effects of exercise on neurogenesis and cognition to the aged brain. *Science* **369**, 167-173, doi:10.1126/science.aaw2622 (2020).

17 Ozek, C., Krolewski, R. C., Buchanan, S. M. & Rubin, L. L. Growth Differentiation Factor 11 treatment leads to neuronal and vascular improvements in the hippocampus of aged mice. *Sci Rep* **8**, 17293, doi:10.1038/s41598-018-35716-6 (2018).

18 Wrann, C. D. *et al.* Exercise induces hippocampal BDNF through a PGC-1α/FNDC5 pathway. *Cell Metab* **18**, 649-659, doi:10.1016/j.cmet.2013.09.008 (2013).

19 Islam, M. R. *et al.* Exercise hormone irisin is a critical regulator of cognitive function. *Nature Metabolism* **3**, 1058-1070, doi:10.1038/s42255-021-00438-z (2021).

20 Moon, H. Y. *et al.* Running-Induced Systemic Cathepsin B Secretion Is Associated with Memory Function. *Cell Metab* **24**, 332-340, doi:10.1016/j.cmet.2016.05.025 (2016).

21 White, P. J. *et al.* Protectin DX alleviates insulin resistance by activating a myokine-liver glucoregulatory axis. *Nature Medicine* **20**, 664-669, doi:10.1038/nm.3549 (2014).

1273 22 Quinn, L. S., Anderson, B. G., Strait-Bodey, L., Stroud, A. M. & Argilés, J. M. Oversecretion of
1274 interleukin-15 from skeletal muscle reduces adiposity. *American Journal of Physiology-*
1275 *Endocrinology and Metabolism* **296**, E191-E202 (2009).
1276 23 Lourenco, M. V. *et al.* Exercise-linked FNDC5/irisin rescues synaptic plasticity and memory
1277 defects in Alzheimer's models. *Nat Med* **25**, 165-175, doi:10.1038/s41591-018-0275-4 (2019).
1278 24 Gupta, R., Khan, R. & Cortes, C. J. Forgot to Exercise? Exercise Derived Circulating Myokines in
1279 Alzheimer's Disease: A Perspective. *Front Neurol* **12**, 649452, doi:10.3389/fneur.2021.649452
1280 (2021).
1281 25 Boyle, P. A., Buchman, A. S., Wilson, R. S., Leurgans, S. E. & Bennett, D. A. Association of muscle
1282 strength with the risk of Alzheimer disease and the rate of cognitive decline in community-
1283 dwelling older persons. *Arch Neurol* **66**, 1339-1344, doi:10.1001/archneurol.2009.240 (2009).
1284 26 Kim, J. *et al.* Association of muscle and visceral adipose tissues with the probability of
1285 Alzheimer's disease in healthy subjects. *Sci Rep* **9**, 949, doi:10.1038/s41598-018-37244-9 (2019).
1286 27 Cortes, C. J. *et al.* Polyglutamine-expanded androgen receptor interferes with TFEB to elicit
1287 autophagy defects in SBMA. *Nat Neurosci* **17**, 1180-1189, doi:10.1038/nn.3787 (2014).
1288 28 Cortes, C. J. *et al.* Muscle expression of mutant androgen receptor accounts for systemic and
1289 motor neuron disease phenotypes in spinal and bulbar muscular atrophy. *Neuron* **82**, 295-307,
1290 doi:10.1016/j.neuron.2014.03.001 (2014).
1291 29 Lieberman, A. P. *et al.* Peripheral androgen receptor gene suppression rescues disease in mouse
1292 models of spinal and bulbar muscular atrophy. *Cell reports* **7**, 774-784,
1293 doi:10.1016/j.celrep.2014.02.008 (2014).
1294 30 Settembre, C. *et al.* TFEB links autophagy to lysosomal biogenesis. *Science* **332**, 1429-1433,
1295 doi:10.1126/science.1204592 (2011).
1296 31 Palmieri, M. *et al.* Characterization of the CLEAR network reveals an integrated control of
1297 cellular clearance pathways. *Hum Mol Genet* **20**, 3852-3866, doi:10.1093/hmg/ddr306 (2011).
1298 32 Sardiello, M. *et al.* A gene network regulating lysosomal biogenesis and function. *Science* **325**,
1299 473-477, doi:10.1126/science.1174447 (2009).
1300 33 Morgan, T. E. *et al.* The mosaic of brain glial hyperactivity during normal ageing and its
1301 attenuation by food restriction. *Neuroscience* **89**, 687-699, doi:10.1016/s0306-4522(98)00334-0
1302 (1999).
1303 34 van Praag, H., Shubert, T., Zhao, C. & Gage, F. H. Exercise enhances learning and hippocampal
1304 neurogenesis in aged mice. *J Neurosci* **25**, 8680-8685, doi:10.1523/jneurosci.1731-05.2005
1305 (2005).
1306 35 Settembre, C. *et al.* TFEB controls cellular lipid metabolism through a starvation-induced
1307 autoregulatory loop. *Nat Cell Biol* **15**, 647-658, doi:10.1038/ncb2718 (2013).
1308 36 Mansueto, G. *et al.* Transcription Factor EB Controls Metabolic Flexibility during Exercise. *Cell*
1309 *Metab* **25**, 182-196, doi:10.1016/j.cmet.2016.11.003 (2017).
1310 37 Leu, M. *et al.* Erbb2 regulates neuromuscular synapse formation and is essential for muscle
1311 spindle development. *Development* **130**, 2291-2301 (2003).
1312 38 Madisen, L. *et al.* A robust and high-throughput Cre reporting and characterization system for
1313 the whole mouse brain. *Nat Neurosci* **13**, 133-140, doi:10.1038/nn.2467 (2010).
1314 39 Masiero, E. *et al.* Autophagy is required to maintain muscle mass. *Cell Metab* **10**, 507-515,
1315 doi:10.1016/j.cmet.2009.10.008 (2009).
1316 40 Kustermann, M. *et al.* Loss of the novel Vcp (valosin containing protein) interactor Washc4
1317 interferes with autophagy-mediated proteostasis in striated muscle and leads to myopathy in
1318 vivo. *Autophagy* **14**, 1911-1927, doi:10.1080/15548627.2018.1491491 (2018).
1319 41 Giacomello, E. *et al.* Age Dependent Modification of the Metabolic Profile of the Tibialis Anterior
1320 Muscle Fibers in C57BL/6J Mice. *Int J Mol Sci* **21**, doi:10.3390/ijms21113923 (2020).

42 Szklarczyk, D. *et al.* The STRING database in 2021: customizable protein-protein networks, and functional characterization of user-uploaded gene/measurement sets. *Nucleic Acids Res* **49**, D605-D612, doi:10.1093/nar/gkaa1074 (2021).
43 Spampanato, C. *et al.* Transcription factor EB (TFEB) is a new therapeutic target for Pompe disease. *EMBO Mol Med* **5**, 691-706, doi:10.1002/emmm.201202176 (2013).
44 Valentine, J. M. *et al.* NFkappaB Regulates Muscle Development and Mitochondrial Function. *J Gerontol A Biol Sci Med Sci* **75**, 647-653, doi:10.1093/gerona/gly262 (2020).
45 Rai, M. & Demontis, F. Systemic Nutrient and Stress Signaling via Myokines and Myometabolites. *Annu Rev Physiol* **78**, 85-107, doi:10.1146/annurev-physiol-021115-105305 (2016).
46 Mancinelli, R. *et al.* Biological Aspects of Selected Myokines in Skeletal Muscle: Focus on Aging. *Int J Mol Sci* **22**, doi:10.3390/ijms22168520 (2021).
47 Cortazar, A. R., Oguiza, J. A., Aransay, A. M. & Lavin, J. L. VerSeDa: vertebrate secretome database. *Database (Oxford)* **2017**, doi:10.1093/database/baw171 (2017).
48 Yoshiyama, Y. *et al.* Synapse loss and microglial activation precede tangles in a P301S tauopathy mouse model. *Neuron* **53**, 337-351, doi:10.1016/j.neuron.2007.01.010 (2007).
49 Moloney, C. M., Lowe, V. J. & Murray, M. E. Visualization of neurofibrillary tangle maturity in Alzheimer's disease: A clinicopathologic perspective for biomarker research. *Alzheimers Dement* **17**, 1554-1574, doi:10.1002/alz.12321 (2021).
50 Jurga, A. M., Paleczna, M. & Kuter, K. Z. Overview of General and Discriminating Markers of Differential Microglia Phenotypes. *Front Cell Neurosci* **14**, 198, doi:10.3389/fncel.2020.00198 (2020).
51 Rozovsky, I., Finch, C. E. & Morgan, T. E. Age-related activation of microglia and astrocytes: in vitro studies show persistent phenotypes of aging, increased proliferation, and resistance to down-regulation. *Neurobiol Aging* **19**, 97-103, doi:10.1016/s0197-4580(97)00169-3 (1998).
52 Godbout, J. P. *et al.* Exaggerated neuroinflammation and sickness behavior in aged mice following activation of the peripheral innate immune system. *FASEB J* **19**, 1329-1331, doi:10.1096/fj.05-3776fje (2005).
53 Sidoryk-Wegrzynowicz, M. *et al.* Astrocytes in mouse models of tauopathies acquire early deficits and lose neurosupportive functions. *Acta Neuropathol Commun* **5**, 89, doi:10.1186/s40478-017-0478-9 (2017).
54 Preuss, C. *et al.* A novel systems biology approach to evaluate mouse models of late-onset Alzheimer's disease. *Mol Neurodegener* **15**, 67, doi:10.1186/s13024-020-00412-5 (2020).
55 Sherva, R. *et al.* Genome-wide association study of the rate of cognitive decline in Alzheimer's disease. *Alzheimers Dement* **10**, 45-52, doi:10.1016/j.jalz.2013.01.008 (2014).
56 Simon, M. J. *et al.* Transcriptional network analysis of human astrocytic endfoot genes reveals region-specific associations with dementia status and tau pathology. *Sci Rep* **8**, 12389, doi:10.1038/s41598-018-30779-x (2018).
57 Knopman, D. S. *et al.* Alzheimer disease. *Nat Rev Dis Primers* **7**, 33, doi:10.1038/s41572-021-00269-y (2021).
58 Guyenet, S. J. *et al.* A simple composite phenotype scoring system for evaluating mouse models of cerebellar ataxia. *J Vis Exp*, doi:10.3791/1787 (2010).
59 Lehallier, B. *et al.* Undulating changes in human plasma proteome profiles across the lifespan. *Nature Medicine* **25**, 1843-1850, doi:10.1038/s41591-019-0673-2 (2019).
60 Jiao, J. & Demontis, F. Skeletal muscle autophagy and its role in sarcopenia and organismal aging. *Curr Opin Pharmacol* **34**, 1-6, doi:10.1016/j.coph.2017.03.009 (2017).
61 Wohlgemuth, S. E., Seo, A. Y., Marzetti, E., Lees, H. A. & Leeuwenburgh, C. Skeletal muscle autophagy and apoptosis during aging: effects of calorie restriction and life-long exercise. *Experimental gerontology* **45**, 138-148, doi:10.1016/j.exger.2009.11.002 (2010).

62 Yu, D. *et al.* The adverse metabolic effects of branched-chain amino acids are mediated by isoleucine and valine. *Cell Metab* **33**, 905-922 e906, doi:10.1016/j.cmet.2021.03.025 (2021).
63 Adler, D. H. *et al.* Characterizing the human hippocampus in aging and Alzheimer's disease using a computational atlas derived from ex vivo MRI and histology. *Proc Natl Acad Sci U S A* **115**, 4252-4257, doi:10.1073/pnas.1801093115 (2018).
64 Ivanisevic, J. *et al.* Metabolic drift in the aging brain. *Aging (Albany NY)* **8**, 1000-1020, doi:10.18632/aging.100961 (2016).
65 Ximerakis, M. *et al.* Single-cell transcriptomic profiling of the aging mouse brain. *Nat Neurosci* **22**, 1696-1708, doi:10.1038/s41593-019-0491-3 (2019).
66 Zarate, S., Stevnsner, T. & Gredilla, R. Role of Estrogen and Other Sex Hormones in Brain Aging. Neuroprotection and DNA Repair. *Front Aging Neurosci* **9**, 430, doi:10.3389/fnagi.2017.00430 (2017).
67 Hahn, O. *et al.* Atlas of the aging mouse brain reveals white matter as vulnerable foci. *Cell*, doi:10.1016/j.cell.2023.07.027 (2023).
68 Cortes, C. J. & De Miguel, Z. Precision Exercise Medicine: Sex Specific Differences in Immune and CNS Responses to Physical Activity. *Brain Plasticity*, pp. 1-13, doi:10.3233/BPL-220139 (2022).
69 Vizovisek, M., Fonovic, M. & Turk, B. Cysteine cathepsins in extracellular matrix remodeling: Extracellular matrix degradation and beyond. *Matrix Biol* **75-76**, 141-159, doi:10.1016/j.matbio.2018.01.024 (2019).
70 Tran, A. P., Sundar, S., Yu, M., Lang, B. T. & Silver, J. Modulation of Receptor Protein Tyrosine Phosphatase Sigma Increases Chondroitin Sulfate Proteoglycan Degradation through Cathepsin B Secretion to Enhance Axon Outgrowth. *J Neurosci* **38**, 5399-5414, doi:10.1523/JNEUROSCI.3214-17.2018 (2018).
71 Saini, M. G. & Bix, G. J. Oxygen-glucose deprivation (OGD) and interleukin-1 (IL-1) differentially modulate cathepsin B/L mediated generation of neuroprotective perlecan LG3 by neurons. *Brain Res* **1438**, 65-74, doi:10.1016/j.brainres.2011.12.027 (2012).
72 Muigg, P. *et al.* Differential stress-induced neuronal activation patterns in mouse lines selectively bred for high, normal or low anxiety. *PLoS One* **4**, e5346, doi:10.1371/journal.pone.0005346 (2009).
73 Czibere, L. *et al.* Profiling trait anxiety: transcriptome analysis reveals cathepsin B (Ctsb) as a novel candidate gene for emotionality in mice. *PLoS One* **6**, e23604, doi:10.1371/journal.pone.0023604 (2011).
74 New, J. & Thomas, S. M. Autophagy-dependent secretion: mechanism, factors secreted, and disease implications. *Autophagy* **15**, 1682-1693, doi:10.1080/15548627.2019.1596479 (2019).
75 Chow, L. S. *et al.* Exerkines in health, resilience and disease. *Nat Rev Endocrinol* **18**, 273-289, doi:10.1038/s41574-022-00641-2 (2022).
76 Schindelin, J. *et al.* Fiji: an open-source platform for biological-image analysis. *Nature Methods* **9**, 676-682, doi:10.1038/nmeth.2019 (2012).
77 Encarnacion-Rivera, L., Foltz, S., Hartzell, H. C. & Choo, H. Myosoft: An automated muscle histology analysis tool using machine learning algorithm utilizing FIJI/ImageJ software. *PLoS One* **15**, e0229041, doi:10.1371/journal.pone.0229041 (2020).
78 Herrera, J. J. *et al.* Acarbose has sex-dependent and -independent effects on age-related physical function, cardiac health, and lipid biology. *JCI Insight* **5**, doi:10.1172/jci.insight.137474 (2020).
79 Amodei, D. *et al.* Improving Precursor Selectivity in Data-Independent Acquisition Using Overlapping Windows. *J Am Soc Mass Spectrom* **30**, 669-684, doi:10.1007/s13361-018-2122-8 (2019).

1416 80 Adusumilli, R. & Mallick, P. Data Conversion with ProteoWizard msConvert. *Methods Mol Biol*
1417 **1550**, 339-368, doi:10.1007/978-1-4939-6747-6_23 (2017).
1418 81 Searle, B. C. *et al.* Chromatogram libraries improve peptide detection and quantification by data
1419 independent acquisition mass spectrometry. *Nat Commun* **9**, 5128, doi:10.1038/s41467-018-
1420 07454-w (2018).
1421 82 Wu, C. H. *et al.* The Universal Protein Resource (UniProt): an expanding universe of protein
1422 information. *Nucleic Acids Res* **34**, D187-191, doi:10.1093/nar/gkj161 (2006).
1423 83 Kall, L., Canterbury, J. D., Weston, J., Noble, W. S. & MacCoss, M. J. Semi-supervised learning for
1424 peptide identification from shotgun proteomics datasets. *Nat Methods* **4**, 923-925,
1425 doi:10.1038/nmeth1113 (2007).
1426 84 MacLean, B. *et al.* Skyline: an open source document editor for creating and analyzing targeted
1427 proteomics experiments. *Bioinformatics* **26**, 966-968, doi:10.1093/bioinformatics/btq054
1428 (2010).
1429 85 Sharma, V. *et al.* Panorama Public: A Public Repository for Quantitative Data Sets Processed in
1430 Skyline. *Mol Cell Proteomics* **17**, 1239-1244, doi:10.1074/mcp.RA117.000543 (2018).
1431 86 Pesta, D. *et al.* Similar qualitative and quantitative changes of mitochondrial respiration
1432 following strength and endurance training in normoxia and hypoxia in sedentary humans. *Am J*
1433 *Physiol Regul Integr Comp Physiol* **301**, R1078-1087, doi:10.1152/ajpregu.00285.2011 (2011).
1434 87 Tomfohr, J., Lu, J. & Kepler, T. B. Pathway level analysis of gene expression using singular value
1435 decomposition. *BMC Bioinformatics* **6**, 225, doi:10.1186/1471-2105-6-225 (2005).

1436

Figure 1

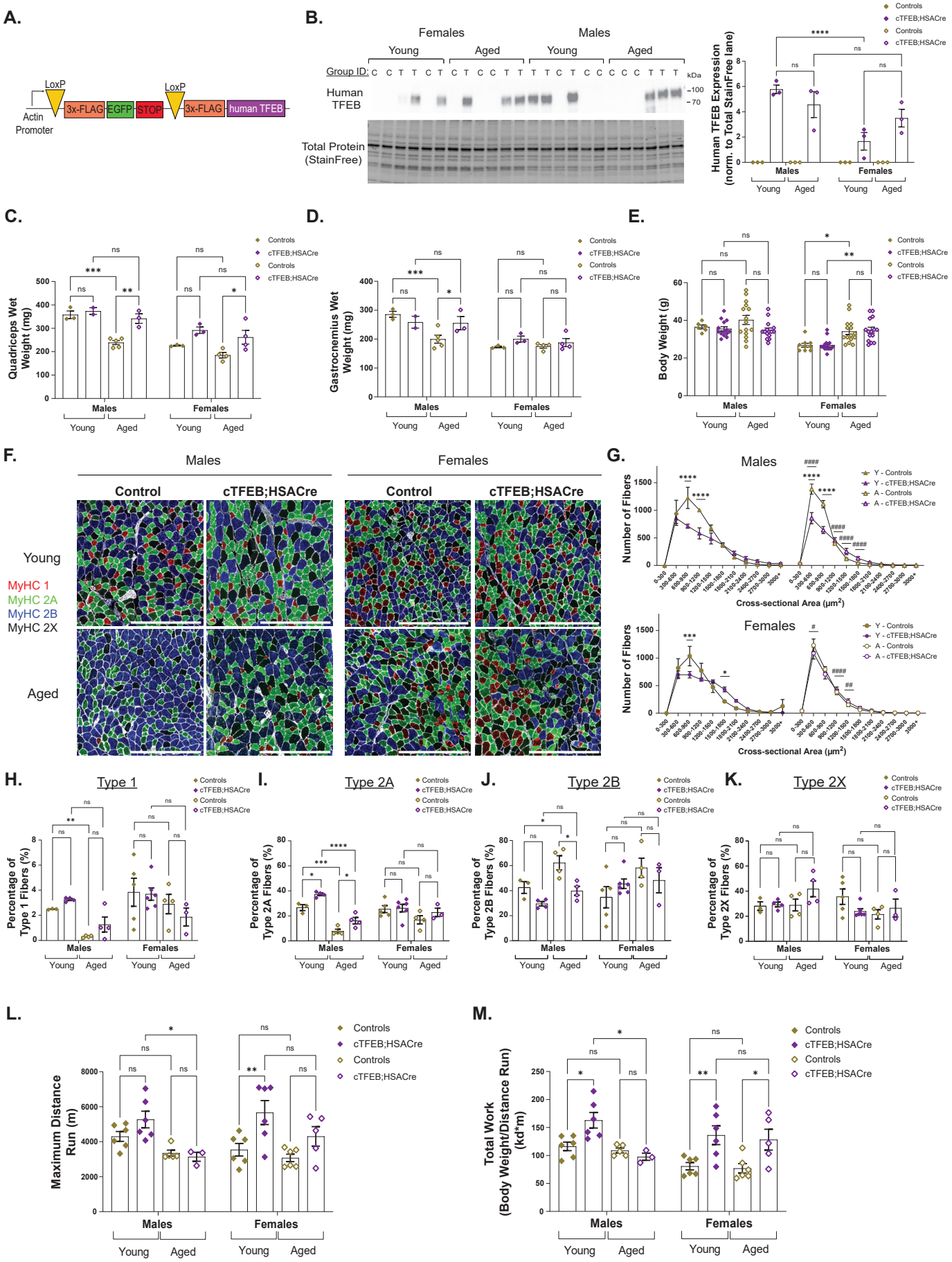
A.
LoxP
LoxP
Actin Promoter
3x-FLAG
EGFP
STOP
3x-FLAG
human TFEB
B.
Females
Males
Young
Aged
Young
Aged
Group ID: C C T T C T C T C C T T T T C T C C C C C T T T
kDa
100
70
Human TFEB
Total Protein (StainFree)
Human TFEB Expression (norm. to Total StainFree lane)
Controls
cTFEB;HSACre
Controls
cTFEB;HSACre
Males
Females
Young
Aged
Young
Aged
C.
Quadriceps Wet Weight (mg)
D.
Gastrocnemius Wet Weight (mg)
E.
Body Weight (g)
F.
Males
Females
Control
cTFEB;HSACre
Control
cTFEB;HSACre
Young
Aged
MyHC 1
MyHC 2A
MyHC 2B
MyHC 2X
G.
Males
Females
Number of Fibers
Cross-sectional Area (μm²)
Y - Controls
Y - cTFEB;HSACre
A - Controls
A - cTFEB;HSACre
H.
Type 1
Percentage of Type 1 Fibers (%)
I.
Type 2A
Percentage of Type 2A Fibers (%)
J.
Type 2B
Percentage of Type 2B Fibers (%)
K.
Type 2X
Percentage of Type 2X Fibers (%)
L.
Maximum Distance Run (m)
M.
Total Work (Body Weight/Distance Run) (kd*m)

Figure 2

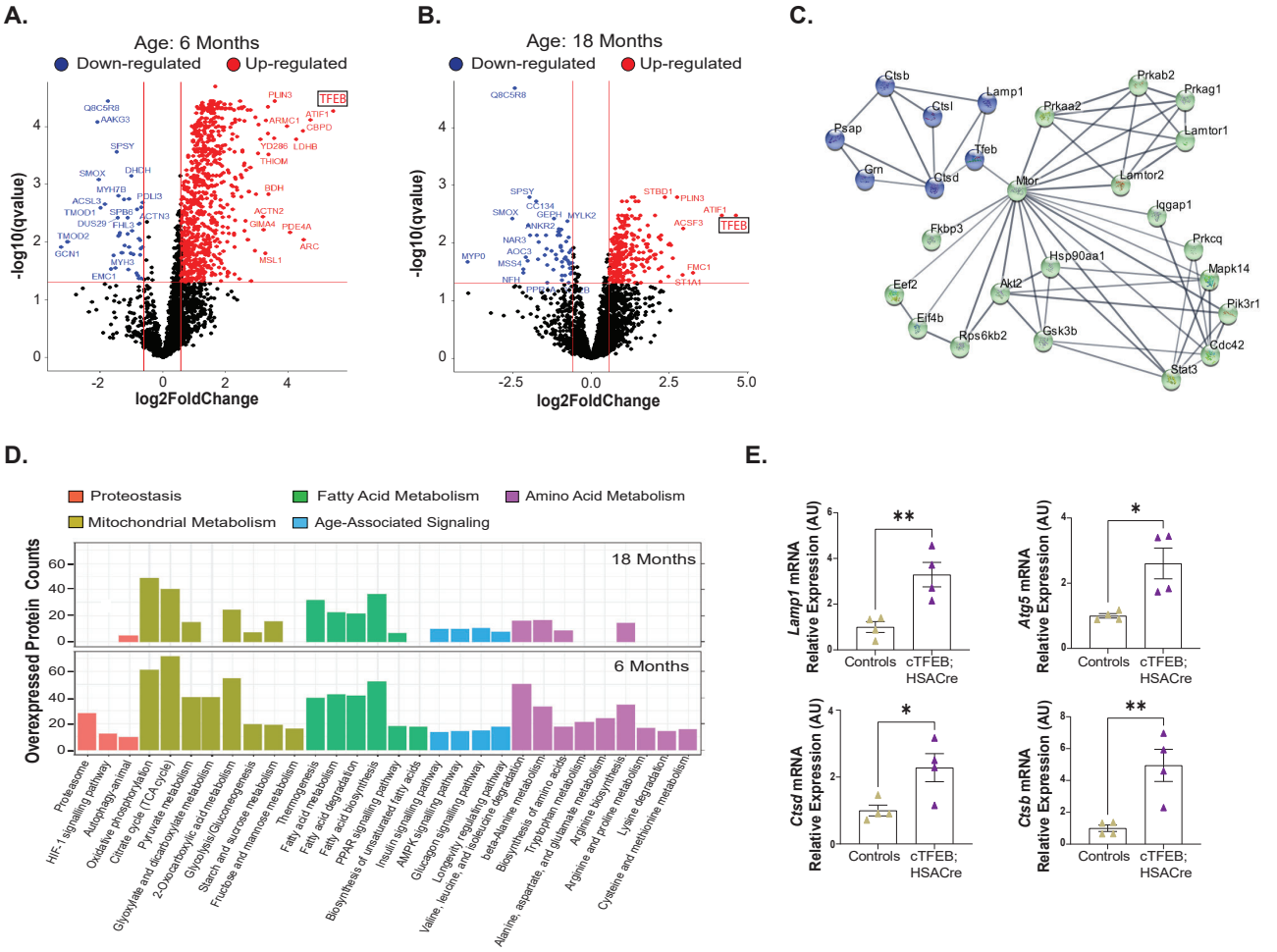
A.
Age: 6 Months
Down-regulated
Up-regulated
-log10(qvalue)
log2FoldChange
TFEB
B.
Age: 18 Months
Down-regulated
Up-regulated
-log10(qvalue)
log2FoldChange
TFEB
C.
Ctsb
Lamp1
Ctsl
Psap
Tfeb
Grn
Ctsd
Mtor
Prkab2
Prkag1
Prkaa2
Lamtor1
Lamtor2
Iqgap1
Fkbp3
Prkcq
Hsp90aa1
Mapk14
Eef2
Akt2
Pik3r1
Eif4b
Rps6kb2
Gsk3b
Cdc42
Stat3
D.
Proteostasis
Fatty Acid Metabolism
Amino Acid Metabolism
Mitochondrial Metabolism
Age-Associated Signaling
Overexpressed Protein Counts
18 Months
6 Months
Proteasome
HIF-1 signalling pathway
Autophagy-animal
Oxidative phosphorylation
Citrate cycle (TCA cycle)
Pyruvate metabolism
Glyoxylate and dicarboxylate metabolism
2-Oxocarboxylic acid metabolism
Glycolysis/Gluconeogenesis
Starch and sucrose metabolism
Fructose and mannose metabolism
Thermogenesis
Fatty acid metabolism
Fatty acid degradation
Fatty acid biosynthesis
PPAR signalling pathway
Biosynthesis of unsaturated fatty acids
Insulin signalling pathway
AMPK signalling pathway
Glucagon signalling pathway
Longevity regulating pathway
Valine, leucine and isoleucine degradation
beta-Alanine metabolism
Biosynthesis of amino acids
Tryptophan metabolism
Alanine, aspartate and glutamate metabolism
Arginine biosynthesis
Arginine and proline metabolism
Lysine degradation
Cysteine and methionine metabolism
E.
Lamp1 mRNA Relative Expression (AU)
Atg5 mRNA Relative Expression (AU)
Ctsd mRNA Relative Expression (AU)
Ctsb mRNA Relative Expression (AU)
Controls
cTFEB; HSACre

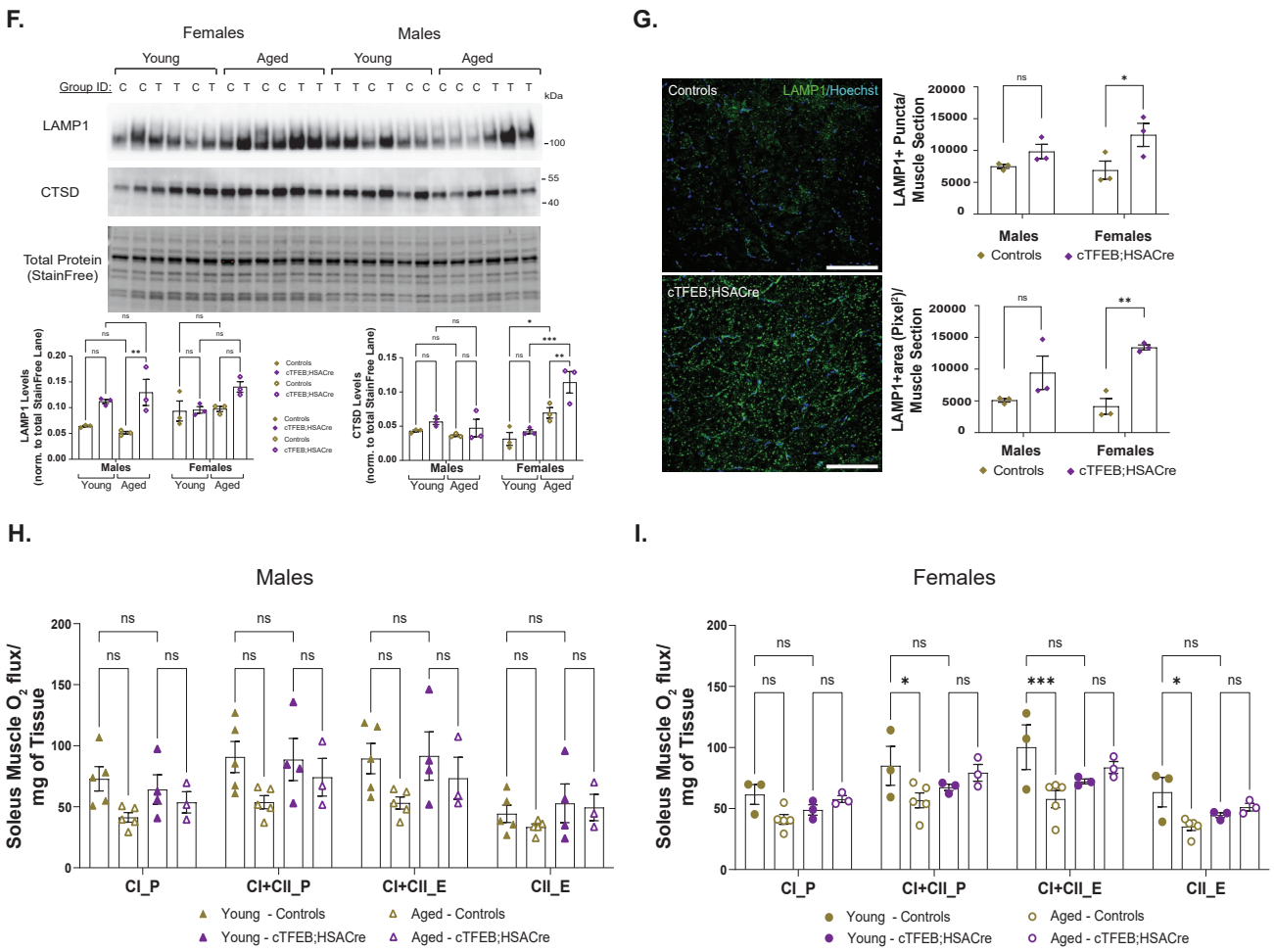
F.
Females
Males
Young
Aged
Group ID:
LAMP1
CTSD
Total Protein (StainFree)
kDa
LAMP1 Levels (norm. to total StainFree Lane)
CTSD Levels (norm. to total StainFree Lane)
Controls
cTFEB;HSACre
G.
Controls
LAMP1/Hoechst
cTFEB;HSACre
LAMP1+ Puncta/ Muscle Section
LAMP1+area (Pixel²)/ Muscle Section
Males
Females
H.
Males
Soleus Muscle O2 flux/ mg of Tissue
CI_P
CI+CII_P
CI+CII_E
CII_E
Young - Controls
Young - cTFEB;HSACre
Aged - Controls
Aged - cTFEB;HSACre
I.
Females

Figure 3

A.

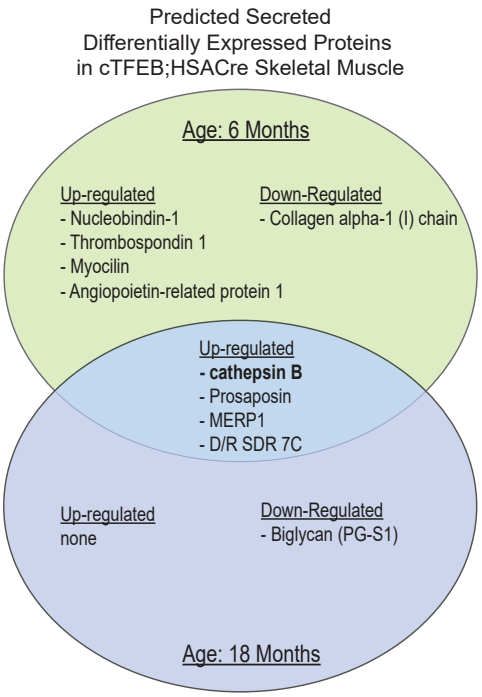
Predicted Secreted
Differentially Expressed Proteins
in cTFEB;HSACre Skeletal Muscle
Age: 6 Months
Up-regulated
- Nucleobindin-1
- Thrombospondin 1
- Myocilin
- Angiopoietin-related protein 1
Down-Regulated
- Collagen alpha-1 (I) chain
Up-regulated
- cathepsin B
- Prosaposin
- MERP1
- D/R SDR 7C
Up-regulated
none
Down-Regulated
- Biglycan (PG-S1)
Age: 18 Months

B.

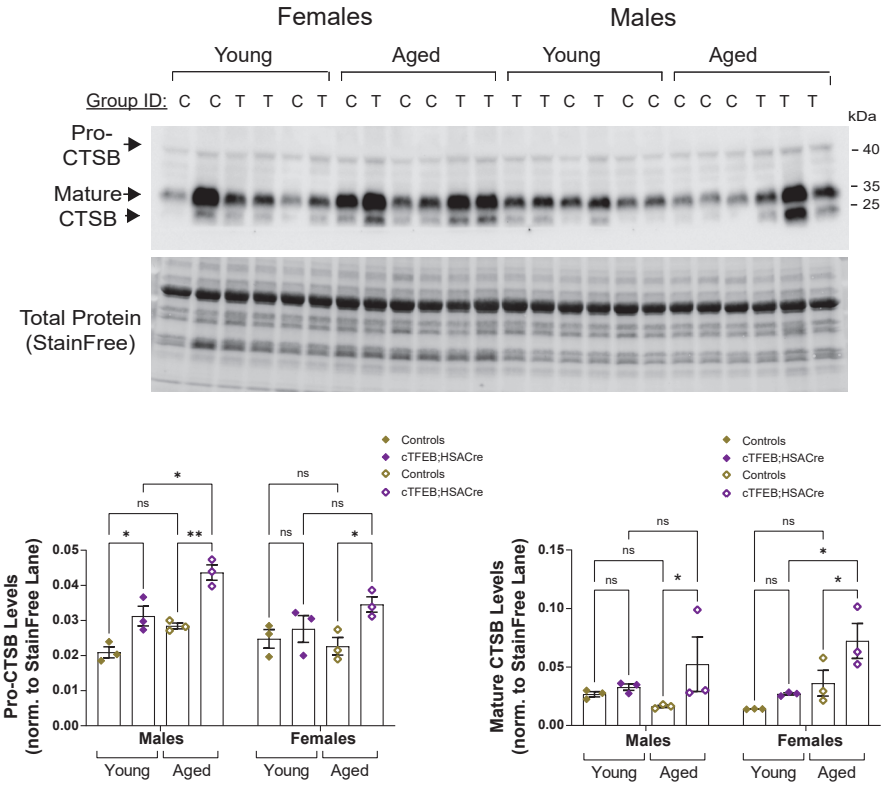
Females
Males
Young
Aged
Young
Aged
Group ID: C C T T C T C T C C T T T T C T C C C C C T T T
kDa
Pro-CTSB
Mature CTSB
40
35
25
Total Protein (StainFree)
Controls
cTFEB;HSACre
Controls
cTFEB;HSACre
Pro-CTSB Levels (norm. to StainFree Lane)
0.05
0.04
0.03
0.02
0.01
0.00
Males
Females
Young
Aged
Young
Aged
Mature CTSB Levels (norm. to StainFree Lane)
0.15
0.10
0.05
0.00
ns
*
**

C.

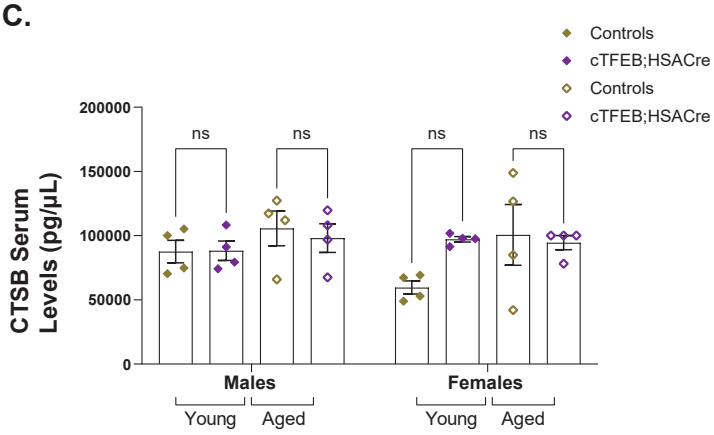
Controls
cTFEB;HSACre
Controls
cTFEB;HSACre
CTSB Serum Levels (pg/µL)
200000
150000
100000
50000
0
ns
Males
Females
Young
Aged
Young
Aged

Figure 4

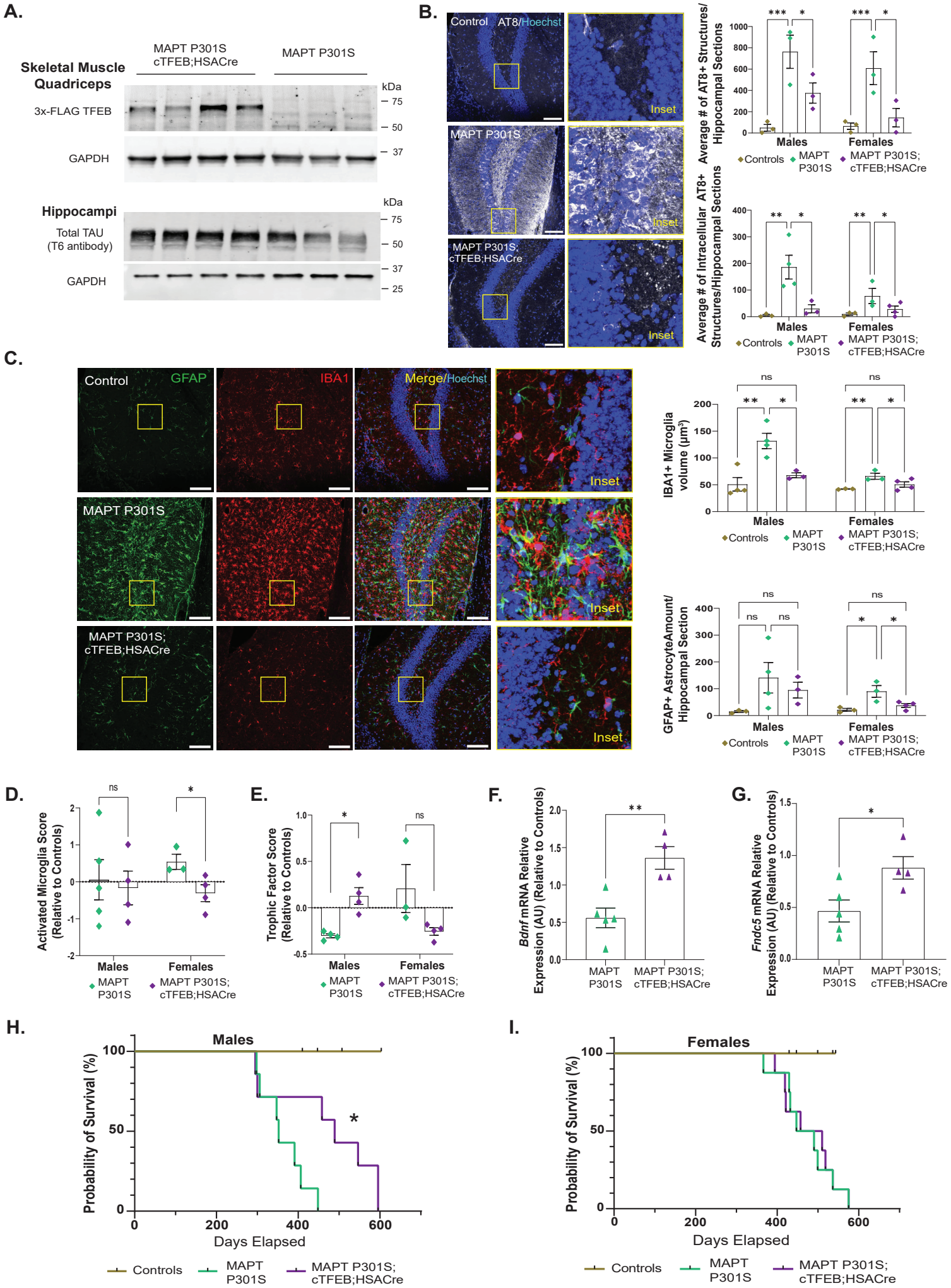
A.
Skeletal Muscle Quadriceps
MAPT P301S cTFEB;HSACre
MAPT P301S
3x-FLAG TFEB
GAPDH
kDa
75
50
37
Hippocampi
Total TAU (T6 antibody)
GAPDH
kDa
75
50
37
25
B.
Control
AT8/Hoechst
Inset
MAPT P301S
MAPT P301S; cTFEB;HSACre
Average # of AT8+ Structures/ Hippocampal Sections
Average # of Intracellular AT8+ Structures/Hippocampal Sections
Males
Females
Controls
MAPT P301S
MAPT P301S; cTFEB;HSACre
C.
Control
GFAP
IBA1
Merge/Hoechst
Inset
MAPT P301S
MAPT P301S; cTFEB;HSACre
IBA1+ Microglia volume (μm³)
GFAP+ AstrocyteAmount/ Hippocampal Section
ns
D.
Activated Microglia Score (Relative to Controls)
E.
Trophic Factor Score (Relative to Controls)
F.
Bdnf mRNA Relative Expression (AU) (Relative to Controls)
G.
Fndc5 mRNA Relative Expression (AU) (Relative to Controls)
H.
Males
Probability of Survival (%)
Days Elapsed
I.
Females
Probability of Survival (%)
Days Elapsed

Figure 5

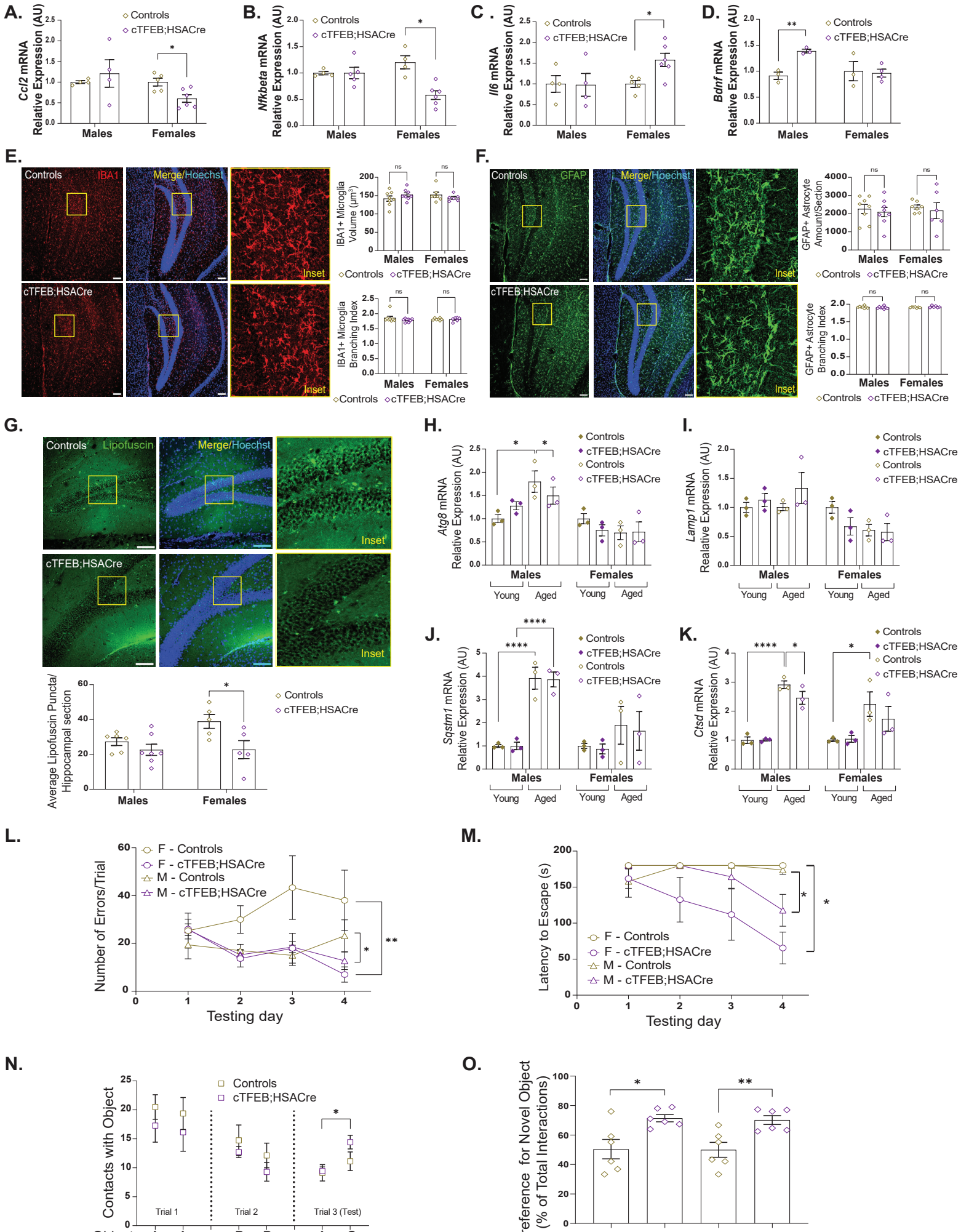
A.
Ccl2 mRNA Relative Expression (AU)
Controls
cTFEB;HSACre
Males
Females
B.
Nfkbeta mRNA Relative Expression (AU)
C.
Il6 mRNA Relative Expression (AU)
D.
Bdnf mRNA Relative Expression (AU)
E.
Controls
IBA1
Merge/Hoechst
Inset
cTFEB;HSACre
IBA1+ Microglia Volume (μm³)
IBA1+ Microglia Branching Index
ns
F.
GFAP
GFAP+ Astrocyte Amount/Section
GFAP+ Astrocyte Branching Index
G.
Lipofuscin
Average Lipofuscin Puncta/ Hippocampal section
H.
Atg8 mRNA Relative Expression (AU)
Young
Aged
I.
Lamp1 mRNA Realative Expression (AU)
J.
Sqstm1 mRNA Relative Expression (AU)
K.
Ctsd mRNA Relative Expression (AU)
L.
F - Controls
F - cTFEB;HSACre
M - Controls
M - cTFEB;HSACre
Number of Errors/Trial
Testing day
M.
Latency to Escape (s)
N.
Contacts with Object
Trial 1
Trial 2
Trial 3 (Test)
Object: A A B B A C
O.
Preference for Novel Object (% of Total Interactions)

Figure 6

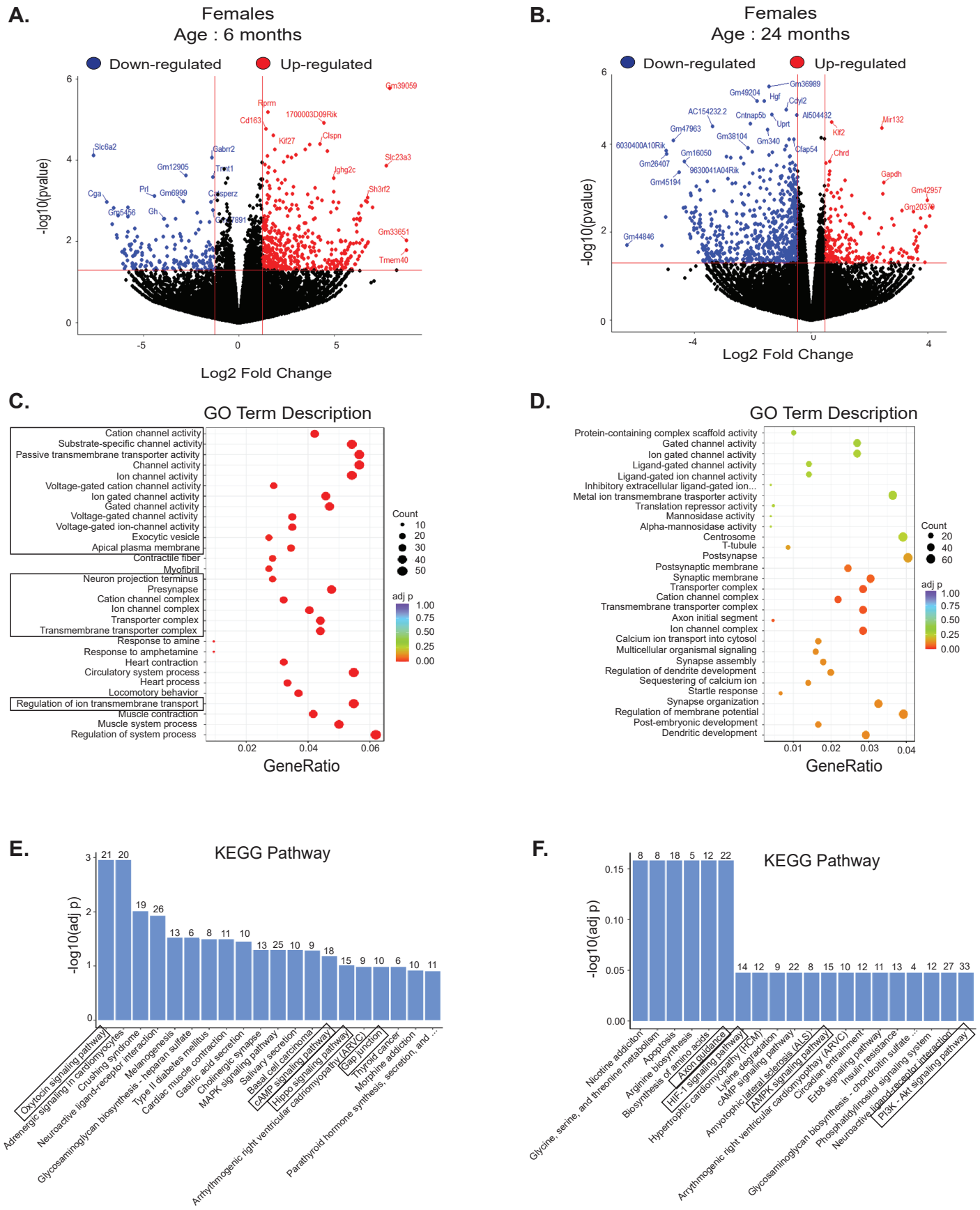
A.
Females
Age : 6 months
Down-regulated
Up-regulated
-log10(pvalue)
Log2 Fold Change
B.
Females
Age : 24 months
Down-regulated
Up-regulated
-log10(pvalue)
Log2 Fold Change
C.
GO Term Description
Cation channel activity
Substrate-specific channel activity
Passive transmembrane transporter activity
Channel activity
Ion channel activity
Voltage-gated cation channel activity
Ion gated channel activity
Gated channel activity
Voltage-gated channel activity
Voltage-gated ion-channel activity
Exocytic vesicle
Apical plasma membrane
Contractile fiber
Myofibril
Neuron projection terminus
Presynapse
Cation channel complex
Ion channel complex
Transporter complex
Transmembrane transporter complex
Response to amine
Response to amphetamine
Heart contraction
Circulatory system process
Heart process
Locomotory behavior
Regulation of ion transmembrane transport
Muscle contraction
Muscle system process
Regulation of system process
GeneRatio
Count
adj p
D.
GO Term Description
Protein-containing complex scaffold activity
Gated channel activity
Ion gated channel activity
Ligand-gated channel activity
Ligand-gated ion channel activity
Inhibitory extracellular ligand-gated ion...
Metal ion transmembrane trasporter activity
Translation repressor activity
Mannosidase activity
Alpha-mannosidase activity
Centrosome
T-tubule
Postsynapse
Postsynaptic membrane
Synaptic membrane
Transporter complex
Cation channel complex
Transmembrane transporter complex
Axon initial segment
Ion channel complex
Calcium ion transport into cytosol
Multicellular organismal signaling
Synapse assembly
Regulation of dendrite development
Sequestering of calcium ion
Startle response
Synapse organization
Regulation of membrane potential
Post-embryonic development
Dendritic development
GeneRatio
Count
adj p
E.
KEGG Pathway
-log10(adj p)
Oxytocin signaling pathway
Adrenergic signaling in cardiomyocytes
Crushing syndrome
Neuroactive ligand-receptor interaction
Melanogenesis
Glycosaminoglycan biosynthesis - heparan sulfate
Type II diabetes mellitus
Cardiac muscle contraction
Gastric acid secretion
Cholinergic synapse
MAPK signaling pathway
Salivary secretion
Basal cell carcinoma
cAMP signaling pathway
Hippo signaling pathway
Arrhythmogenic right ventricular cardiomyopathy (ARVC)
Gap junction
Thyroid cancer
Morphine addiction
Parathyroid hormone synthesis, secretion, and ...
F.
KEGG Pathway
-log10(adj p)
Nicotine addiciton
Glycine, serine, and threonine metabolism
Apoptosis
Arginine biosynthesis
Biosynthesis of amino acids
Axon guidance
HIF-1 signaling pathway
Hypertrophic cardiomyopathy (HCM)
Lysine degradation
cAMP signaling pathway
Amyotophic lateral sclerosis (ALS)
AMPK signaling pathway
Arrythmogenic right ventricular cardiomyopthay (ARVC)
Circadian entrainment
Erb8 signaling pathway
Insulin resistance
Glycosaminoglycan biosynthesis - chondroitin sulfate ...
Phosphatidylinositol signaling system
Neuroactive ligand-receptor interaction
PI3K - Akt signaling pathway

Figure 7

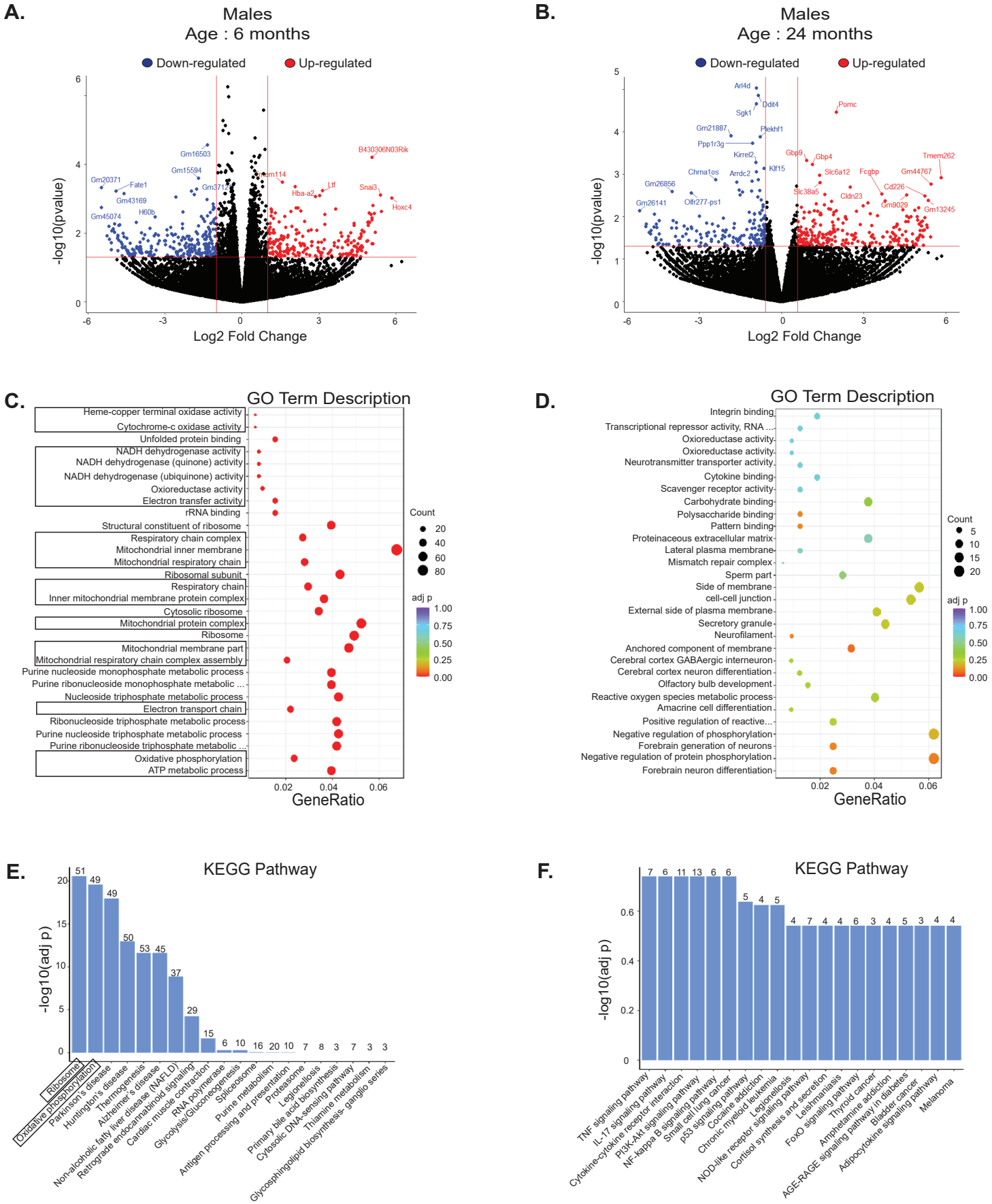
A.
Males
Age : 6 months
Down-regulated
Up-regulated
-log10(pvalue)
Log2 Fold Change
Gm16503
Gm15594
Gm20371
Fate1
Gm43169
Gm45074
H60b
Gm3712
Gm114
Hba-a2
Ltf
Snai3
Hoxc4
B430306N03Rik
B.
Males
Age : 24 months
Down-regulated
Up-regulated
-log10(pvalue)
Log2 Fold Change
Arl4d
Ddit4
Sgk1
Pomc
Gm21887
Plekhf1
Ppp1r3g
Kirrel2
Gbp9
Gbp4
Tmem262
Chrna1os
Arrdc2
Klf15
Slc6a12
Fcgbp
Gm44767
Gm26856
Slc38a5
Cd226
Cldn23
Gm26141
Olfr277-ps1
Gm9029
Gm13245
C.
GO Term Description
Heme-copper terminal oxidase activity
Cytochrome-c oxidase activity
Unfolded protein binding
NADH dehydrogenase activity
NADH dehydrogenase (quinone) activity
NADH dehydrogenase (ubiquinone) activity
Oxioreductase activity
Electron transfer activity
rRNA binding
Structural constituent of ribosome
Respiratory chain complex
Mitochondrial inner membrane
Mitochondrial respiratory chain
Ribosomal subunit
Respiratory chain
Inner mitochondrial membrane protein complex
Cytosolic ribosome
Mitochondrial protein complex
Ribosome
Mitochondrial membrane part
Mitochondrial respiratory chain complex assembly
Purine nucleoside monophosphate metabolic process
Purine ribonucleoside monophosphate metabolic ...
Nucleoside triphosphate metabolic process
Electron transport chain
Ribonucleoside triphosphate metabolic process
Purine nucleoside triphosphate metabolic process
Purine ribonucleoside triphosphate metabolic ...
Oxidative phosphorylation
ATP metabolic process
GeneRatio
Count
adj p
D.
GO Term Description
Integrin binding
Transcriptional repressor activity, RNA ...
Oxioreductase activity
Oxioreductase activity
Neurotransmitter transporter activity
Cytokine binding
Scavenger receptor activity
Carbohydrate binding
Polysaccharide binding
Pattern binding
Proteinaceous extracellular matrix
Lateral plasma membrane
Mismatch repair complex
Sperm part
Side of membrane
cell-cell junction
External side of plasma membrane
Secretory granule
Neurofilament
Anchored component of membrane
Cerebral cortex GABAergic interneuron
Cerebral cortex neuron differentiation
Olfactory bulb development
Reactive oxygen species metabolic process
Amacrine cell differentiation
Positive regulation of reactive...
Negative regulation of phosphorylation
Forebrain generation of neurons
Negative regulation of protein phosphorylation
Forebrain neuron differentiation
GeneRatio
Count
adj p
E.
KEGG Pathway
-log10(adj p)
Ribosome
Oxidative phosphorylation
Parkinson's disease
Huntington's disease
Thermogenesis
Alzheimer's disease
Non-alcoholic fatty liver disease (NAFLD)
Retrograde endocannabinoid signaling
Cardiac muscle contraction
RNA polymerase
Glycolysis/Gluconeogenesis
Spliceosome
Purine metabolism
Antigen processing and presentation
Proteasome
Legionellosis
Primary bile acid biosynthesis
Cytosolic DNA-sensing pathway
Thiamine metabolism
Glycosphingolipid biosynthesis- ganglio series
F.
KEGG Pathway
-log10(adj p)
TNF signaling pathway
IL-17 signaling pathway
Cytokine-cytokine receptor interaction
PI3K-Akt signaling pathway
NF-kappa B signaling pathway
Small cell lung cancer
p53 signaling pathway
Cocaine addiction
Chronic myeloid leukemia
Legionellosis
NOD-like receptor signaling pathway
Cortisol synthesis and secretion
Leishmaniasis
FoxO signaling pathway
Thyroid cancer
Amphetamine addiction
AGE-RAGE signaling pathway in diabetes
Bladder cancer
Adipocytokine signaling pathway
Melanoma